

Spring 5-31-2015

## Modeling of electrical behavior of graphene-based ultracapacitors

Patrick Dzisah  
*New Jersey Institute of Technology*

Follow this and additional works at: <https://digitalcommons.njit.edu/theses>



Part of the [Materials Science and Engineering Commons](#)

---

### Recommended Citation

Dzisah, Patrick, "Modeling of electrical behavior of graphene-based ultracapacitors" (2015). *Theses*. 227.  
<https://digitalcommons.njit.edu/theses/227>

This Thesis is brought to you for free and open access by the Electronic Theses and Dissertations at Digital Commons @ NJIT. It has been accepted for inclusion in Theses by an authorized administrator of Digital Commons @ NJIT. For more information, please contact [digitalcommons@njit.edu](mailto:digitalcommons@njit.edu).

## **Copyright Warning & Restrictions**

The copyright law of the United States (Title 17, United States Code) governs the making of photocopies or other reproductions of copyrighted material.

Under certain conditions specified in the law, libraries and archives are authorized to furnish a photocopy or other reproduction. One of these specified conditions is that the photocopy or reproduction is not to be “used for any purpose other than private study, scholarship, or research.” If a user makes a request for, or later uses, a photocopy or reproduction for purposes in excess of “fair use” that user may be liable for copyright infringement,

This institution reserves the right to refuse to accept a copying order if, in its judgment, fulfillment of the order would involve violation of copyright law.

**Please Note: The author retains the copyright while the New Jersey Institute of Technology reserves the right to distribute this thesis or dissertation**

Printing note: If you do not wish to print this page, then select “Pages from: first page # to: last page #” on the print dialog screen

The Van Houten library has removed some of the personal information and all signatures from the approval page and biographical sketches of theses and dissertations in order to protect the identity of NJIT graduates and faculty.

## **ABSTRACT**

### **MODELING OF ELECTRICAL BEHAVIOR OF GRAPHENE-BASED ULTRACAPACITORS**

**by  
Patrick Dzisah**

Graphene has been identified as a promising material for energy storage, especially for high performance ultracapacitors. Graphene-based ultracapacitors show high stability, significantly-improved capacitance and energy density with fast charging and discharging time at a high current density, due to enhanced ionic electrolyte accessibility in deeper regions. The surface area of a single graphene sheet is  $2630 \text{ m}^2/\text{g}$ , substantially higher than values derived from Brunauer Emmett Teller (BET) surface area measurements of activated carbons used in the current electrochemical double layer capacitors.

In an ultracapacitor cell, chemically modified graphene (CMG) materials demonstrate high specific capacitances of 135 and 99 F/g in aqueous and organic electrolytes, respectively. In addition, high electrical conductivity gives these materials consistently good performance over a wide range of voltage scan rates.

This paper reports a modeling methodology to predict the electrical behavior of a 2.7 V/650 F ultracapacitor cell. The ultracapacitor cell is subject to the charge/discharge cycling with constant-current between 1.35 V and 2.7 V. The charge/discharge current values examined are 50, 100, 150, and 200 A. A three resistor-capacitor (RC) parallel branch model is employed to calculate the electrical behavior of the ultracapacitor. The simulation results for the variations of the cell voltage as a function of time for various charge/discharge currents are in good agreement with the experimental measurements.

**MODELING OF ELECTRICAL BEHAVIOR OF GRAPHENE-BASED  
ULTRACAPACITORS**

**By**

**Patrick Dzisah**

**A Thesis  
Submitted to the Faculty of  
New Jersey Institute of Technology  
in Partial Fulfillment of the Requirements for the Degree of  
Master of Science in Materials Science and Engineering  
Interdisciplinary Program in Materials Science and Engineering**

**May 2011**

Blank Page

**APPROVAL PAGE**

**MODELING OF ELECTRICAL BEHAVIOR OF GRAPHENE-BASED  
ULTRACAPACITORS**

**Patrick Dzisah**

---

Dr. N.M. Ravindra, Thesis Advisor Date  
Professor and Director of Materials Science and Engineering Program, NJIT

---

Dr. Michael Jaffe, Committee Member Date  
Research Professor, Department of Biomedical Engineering, NJIT

---

Dr. Halina Opyrchal, Committee Member Date  
Senior University Lecturer, Department of Physics, NJIT

---

Mr. B.S Mani, Committee Member Date  
University Lecturer, Department of Mechanical & Industrial Engineering, NJIT

---

Dr. Willis B. Hammond, Committee Member Date  
CEO, W. B. Hammond Associates, LLC

## **BIOGRAPHICAL SKETCH**

**Author:** Patrick Dzisah  
**Degree:** Master of Science  
**Date:** May 2015

### **Undergraduate and Graduate Education:**

- Master of Science in Material Science and Engineering,  
New Jersey Institute of Technology, Newark, NJ, 2015
- Bachelor of Science in Physics,  
University of Cape Coast, Cape Coast, Ghana, 2008

**Major:** Physics

In the loving memory of my Parents, Brothers and Sisters, Daughter; Lillian Mawuli Dzisah and friends and family for all their support and encouragement.

## ACKNOWLEDGMENTS

I would like to express my sincere gratitude to my advisor Dr Nuggehalli M. Ravindra, for the continuous support he provided me during my Master's study and research. His patience, motivation, enthusiasm and fatherly love, along with his immense knowledge and guidance helped me throughout the time of the research and writing of this thesis. He became my mentor, friend and family.

I would like to thank committee members, Dr. Michael Jaffe, Dr. Halina Opyrchal, Mr. B.S Mani and Dr. Willis B. Hammond for their encouragement, insightful comments, and questions during my defense.

Lastly, I would like to thank all my friends and fellow colleagues: Chang Ge, Yan (Julia) Chu, Hans Tanis and Yang Zunjian for their comments, insights, ideas and support for my simulations.

# TABLE OF CONTENTS

<b>Chapter</b>	<b>Page</b>
1 INTRODUCTION.....	1
1.1 Introduction .....	1
1.2 Outline .....	1
2 FUNDAMENTALS OF ULTRACAPACITORS .....	3
2.1 Introduction to Conventional Capacitors .....	3
2.2 Introduction to Ultracapacitors .....	5
2.2.1 Basic Operation Principle.....	6
2.2.2 Ultracapacitor Cell Construction .....	9
2.2.3 Electrodes .....	11
2.2.4 Electrolyte.....	12
2.2.5 Ultracapacitor Charge Separation .....	14
2.3 Classifications of Ultracapacitors .....	16
2.3.1 Electrochemical Double-Layer Capacitors .....	17
2.3.2 Pseudocapacitors .....	18
2.3.3 Hybrid Capacitors .....	18
3 FUNDAMENTALS OF GRAPHENE-BASED ULTRACAPACITORS .....	19
3.1 Introduction.....	19
3.2 Material Candidates for Ultracapacitors Electrodes.....	19
3.2.1 Carbon Materials as non-Faradaic Electrodes .....	20
3.2.1.1 Activated Carbon as Electrode .....	20

**TABLE OF CONTENTS**  
**(Continued)**

<b>Chapter</b>	<b>Page</b>
3.2.1.2 Carbon Aerogels as Electrode .....	21
3.2.1.3 Carbon Nanotubes (CNT) as Electrodes.....	21
3.2.1.4 Graphene as Electrodes.....	23
3.2.2 Pseudocapacitive Materials as Faradaic Electrodes .....	25
3.2.2.1 Metal Oxide.....	25
3.2.2.2 Conducting Polymers.....	26
3.2.2.3 Composite.....	27
3.2.2.4 Asymmetric.....	28
3.2.2.5 Battery-Type.....	28
3.3 Fabrication Techniques for Graphene-Based Electrodes .....	30
3.3.1 Lithography-Based Technique.....	30
3.3.2 Inkjet Printing Technique.....	31
3.3.3 Femtosecond Laser Writing Technique.....	31
3.3.4 Micro-Molding in Capillary (MIMIC) Technique.....	32
3.3 Properties of Graphene-Based Electrodes .....	33
3.4.1 Mechanical Properties of Graphene.....	33
3.4.2 Thermal Properties.....	38
3.4.3 Electrical Properties.....	41

**TABLE OF CONTENTS**  
**(Continued)**

<b>Chapter</b>	<b>Page</b>
3.4.3.1 Hall Effect.....	43
3.5 Joule Heating Effects in Graphene-Based Ultracapacitors.....	45
4 DEVICE MODELING, SIMULATION AND DISCUSSION.....	47
4.1 Introduction.....	47
4.2 Proposed Electric Model for Ultracapacitors.....	48
4.3 Simulation Environment.....	51
4.4 Mathematical Model.....	51
4.5 Results and Discussion.....	54
4.5.1 Varying Voltage Test Results.....	58
5 CONCLUSIONS AND FUTURE WORK .....	59
5.1 Summary.....	59
REFERENCES .....	61

## LIST OF TABLES

<b>Table</b>	<b>Page</b>
2.1 Ultracapacitor Charge Separation.....	15
3.1 Summary of carbon-based ultracapacitors .....	24
3.2 Summary of pseudocapacitive ultracapacitor performance .....	29
3.3 Approximate Young's modulus for various materials.....	35
4.1 Parameters used to calculate the electrical behavior of the ultracapacitor.....	54

## LIST OF FIGURES

<b>Figure</b>	<b>Page</b>
2.1 Schematic of a conventional capacitor .....	4
2.2 Ultracapacitor structure .....	7
2.3 Process that takes place near the carbon surface of an ultracapacitor.....	8
2.4 Ragone plot displaying the energy and power properties.....	9
2.5 Internal Cell Construction .....	10
2.6 Cell Construction .....	10
2.7 Schematic representation of ultracapacitor cell.....	11
2.8 Ultracapacitor Charge Separations .....	15
2.9 Hierarchy of Ultracapacitors.....	16
3.1 A lattice with a positive Poisson's ratio.....	36
3.2 Dependence of Strength and Toughness on Graphene sheet size.....	37
3.3 Thermal Conductivity of Graphene.....	40
3.4 Hall Bar geometry.....	44
3.5 The Quantum Hall Effect in single layer graphene.....	45
4.1 General electric model of ultracapacitor (Ladder Network).....	49
4.2 Three resistor-capacitor (RC) parallel branch model.....	50
4.3 User interface for Simulink.....	51
4.4 Comparison between the modeling results and experimental data.....	56

**LIST OF FIGURES  
(Continued)**

<b>Figure</b>	<b>Page</b>
4.5 Charge/Discharge Curve for graphene ultracapacitor.....	57
4.6 Current-Voltage Curves of graphene-based ultracapacitor.....	57
4.7 Voltage curve for multiple voltages and currents simulation.....	58

# **CHAPTER 1**

## **INTRODUCTION**

### **1.1 Introduction**

Superior electrical conductivity, super chemical stability, high thermal conductivity, mechanical flexibility, and large surface area makes graphene an attractive material for designing ultracapacitor electrodes called Graphene-based electrodes. The recent discovery of graphene- atomically thin layer structure of graphite- has emerged as a unique morphology carbon material with potential for electrochemical energy storage device applications.

In this study, modeling and simulation of graphene-based ultracapacitors are discussed. Also, recent developments in Graphene-based ultracapacitors research are examined with particular focus on the electrochemical performance of graphene-based electrode materials. The modeling and simulation focuses on Electrical Behavior of ultracapacitors using Equivalent Circuit Model.

### **1.2 Outline**

This thesis focuses on the design and simulation of graphene-based ultracapacitors utilizing Three Order Ladder Network (Transmission Line) Model.

In Chapter 2, the fundamentals of Ultracapacitors are discussed. This chapter highlights structural differences between conventional capacitors and ultracapacitors as well as their charge separation mechanisms. Also, various classes of ultracapacitors such as Electric Double-Layer capacitors, Pseudocapacitors and Hybrid capacitors are discussed.

In Chapter 3, the device under consideration in this study - graphene as an ultracapacitor electrode material is introduced. This chapter also discusses material candidates for ultracapacitor electrode design, fabrication techniques used in graphene-based electrode design, properties of graphene as electrode material, and Joule heating in ultracapacitors.

Chapter 4 presents an analysis of the major quantitative modeling research areas concerning the optimization of graphene-based ultracapacitors using the theory discussed in Chapters 2 and 3. Device modeling and simulation results are also discussed. The simulation takes into account quantitative modeling of electrical behavior of ultracapacitors.

Chapter 5 contains conclusions of the present study which presents a summary of the results obtained along with the future work and development of the graphene-based ultracapacitor designs.

## CHAPTER 2

### FUNDAMENTALS OF ULTRACAPACITORS

#### 2.1 Introduction to Conventional Capacitors

Conventional capacitors consist of two conducting electrodes separated by an insulating dielectric material. When a voltage is applied to a capacitor, opposite charges accumulate on the surfaces of each electrode. The charges are kept separate by the dielectric, thus producing an electric field that allows the capacitor to store energy. This is illustrated in Figure 2.1

Capacitance  $C$  is defined as the ratio of stored (positive) charge  $Q$  to the applied voltage  $V$ :

$$C = \frac{Q}{V} \quad (2.1)$$

For a conventional capacitor,  $C$  is directly proportional to the surface area  $A$ , of each electrode and inversely proportional to the distance  $d$ , between the electrodes:

$$C = \epsilon_0 \epsilon_r \frac{A}{d} \quad (2.2)$$

The product of the first two factors on the right hand side of equation (2.2) is a constant of proportionality where,  $\epsilon_0$  is the dielectric constant or permittivity of free space and  $\epsilon_r$  is the dielectric constant of the insulating material between the electrodes.

The two primary attributes of a capacitor are its energy density and power density. For either measure, the density can be calculated as a quantity per unit mass or per unit volume. The energy  $E$  stored in a capacitor is directly proportional to its capacitance:

$$E = \frac{1}{2}CV^2 \quad (2.3)$$

In general, the power  $P$  is the energy expended per unit time. To determine  $P$  for a capacitor, though, one must consider that capacitors are generally represented as a circuit in series with an external “load” resistance  $R$ , as is shown in Figure 2.1.

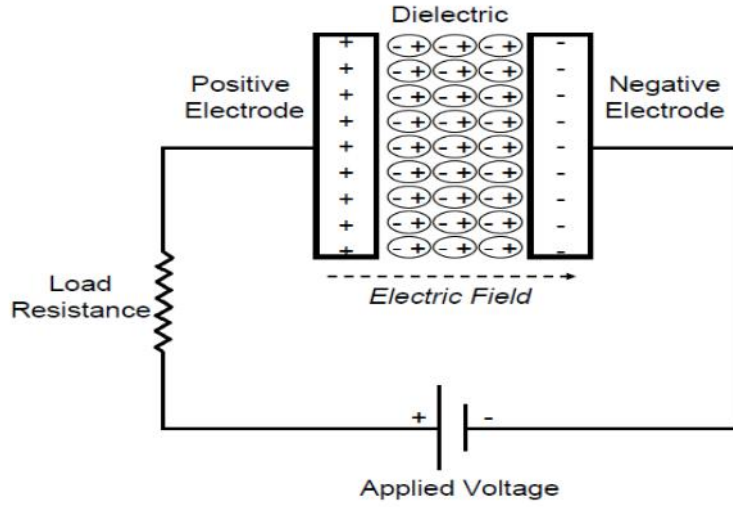


**Figure 2.1** Schematic of a conventional capacitor.  
Source: [6].

The internal components of the capacitor (e.g., current collectors, electrodes, and dielectric material) also contribute to the resistance, which is measured in aggregate by a quantity known as the equivalent series resistance (ESR). The voltage during discharge is determined by these resistances [6] is given by:

$$P_{max} = \frac{V^2}{4 \times ESR} \quad (2.4)$$

This relationship shows how the ESR can limit the maximum power of a capacitor.

Conventional capacitors have relatively high power densities, but relatively low energy densities when compared to electrochemical batteries and to fuel cells. That is, a battery can store more total energy than a capacitor, but it cannot deliver it very quickly,

which means that its power density is low. Capacitors, on the other hand, store relatively less energy per unit mass or volume, but what electrical energy they do store can be discharged rapidly to produce a lot of power, so their power density is usually high.

## **2.2 Introduction to Ultracapacitors**

The need to store and use energy on diverse scales in a modern technological society necessitates the design of large and small energy systems, among which electrical energy storage systems such as batteries and ultracapacitors have attracted much interest in the past several decades [7]. Electric double-layer capacitors, also known as supercapacitors, electrochemical double layer capacitors (EDLCs), ultracapacitors or electrochemical capacitors, with fast power delivery and long cycle life, are energy storage devices that play an important role in complementing or even replacing batteries in many applications [8]. Ultracapacitors offer the promise to supplement batteries and fuel cells in hybrid electric vehicles in providing the necessary power needed during vehicle acceleration and capture energy during regenerative braking. At cruising speeds, a fuel-efficient engine charges the ultracapacitor and provides the power needed for propulsion [6].

Compared to batteries, ultracapacitors normally hold rather high coulometric efficiency (that is, charge/discharge efficiency) and energy efficiency. Ultracapacitors provide higher power density than batteries and fuel cells and higher energy density than conventional capacitors, while offering long lifetimes. The difference is due to different mechanism of energy storage [6]. Batteries store energy by Redox reactions in the bulk electrode, leading to high energy density but slow kinetics. The higher rate capability of ultracapacitors is due to the electrostatic storage of charge at the electrode surface. The

transport of ions in the solution to the electrode surface is rapid, leading to fast charge and discharge capability. In contrast to batteries, no electron transfer takes place across the interface. Ultracapacitors can be fully charged or discharged within a few seconds without damaging the cell and thus are well suited for use in power-assistance applications in hybrid power-train systems. The charging and discharging processes are highly reversible and do not require phase changes in the electrode.

### **2.2.1 Basic Operation Principle**

Ultracapacitors are governed by the same basic principles as conventional capacitors. However, they incorporate electrodes with much higher surface areas  $A$  and much thinner dielectrics that decrease the distance  $d$  between the electrodes. Thus, from Equations (2.2) and (2.3), this leads to an increase in both capacitance and energy. When ultracapacitor is charged, the electrons at the cathode attract positive ions and on the anode the vacancies of electrons attract negative ions in order to locally obtain a charged balance. This attraction of ions leads to a capacitance being formed between the ions and the surface of the electrode. The name dual layer comes from the two layers of ions at each electrode. The layer closest to the electrode acts as a dielectric and the layer outside the first layer hold the charges [7]. This occurs at both electrodes in the ultracapacitor and the total capacitance consists of these two capacitances connected in series. When charges attract ions, they are gathered at the electrode surface. This is shown in Figure 2.2 which is an ideal case. The figure also describes the charged state of all the ions at their respective electrodes. In reality, the diffusion causes some ions to be located at varying distances around the electrodes [7]. The intensity of the electric field determines

the concentration of ions at the electrodes, which means that an increased voltage results in an increased capacitance.

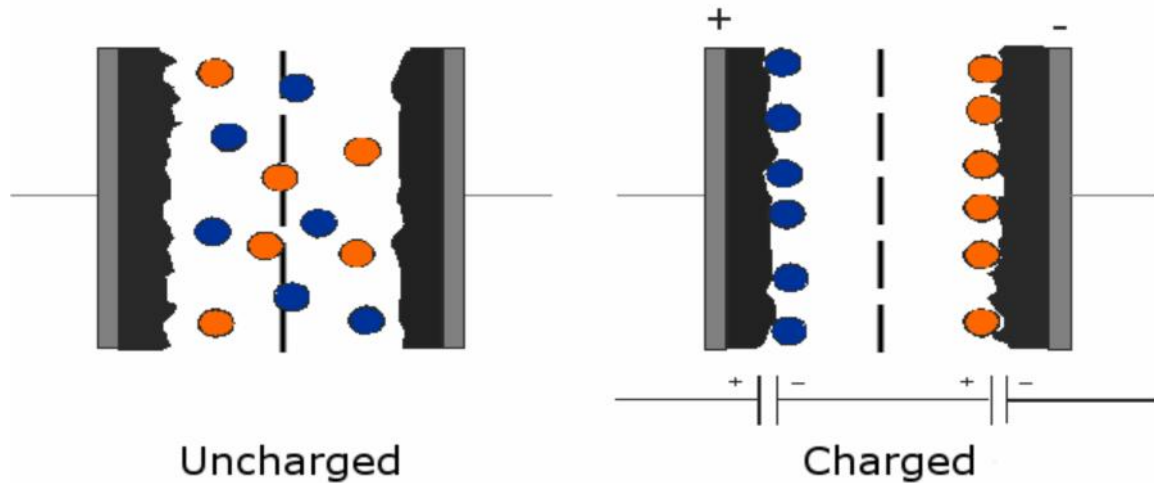


**Figure 2.2** Ultracapacitor structure, red circles describe positive ions and blue describes negative ions.  
Source: [7].

Outside the carbon surface there are two layers, the inner layer consists of non-conducting molecules from the electrolyte. The outer layer consists of ions surrounded by electrolyte molecules. The distance between the carbon surface and the ions is similar to the distance between the electrodes that exist in an ordinary capacitor. Figure 2.3 shows an illustration of this process near the cathode side of the ultracapacitor, a similar process occurs at the anode.

This means that the capacitance is dependent on the ion concentration at the electrodes and the carbon surface area. Since the surface area is extremely large and the distance between the surface and ions is very short, this combination results in a large capacitance [7]. This relation is explained by equation (2.2)

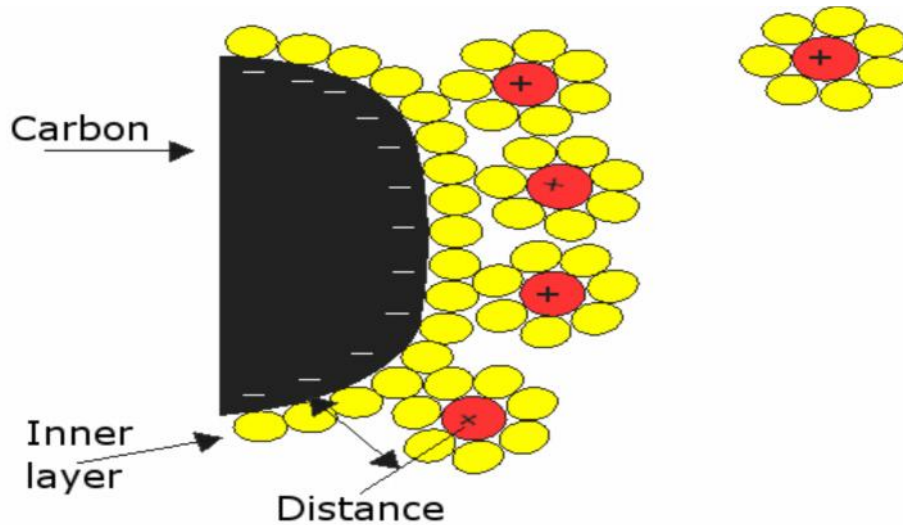


**Figure 2.3** Process that takes place near the carbon surface of an ultracapacitor. The yellow circles describe the electrolyte molecules and the red describe the positive ions. Source: [7].

Furthermore, by maintaining the low ESR characteristic of conventional capacitors, ultracapacitors also are able to achieve comparable high power densities. This can be seen in Figure 2.4 which is a Ragone plot of different electric energy storages. The area which represents fuel cells is valid for systems including the hydrogen storage. The battery area is an average of the most common battery types such as Li-Ion and NiMH. Another difference is the principles upon which they are built (Johansson and Andersson 2008) [7,17-18]. Batteries use chemical processes to store energy which can then be released as electricity. Ultracapacitors, on the other hand, store energy through charge separation. This means that the need for chemicals is reduced, which enables a longer life length of ultracapacitors.

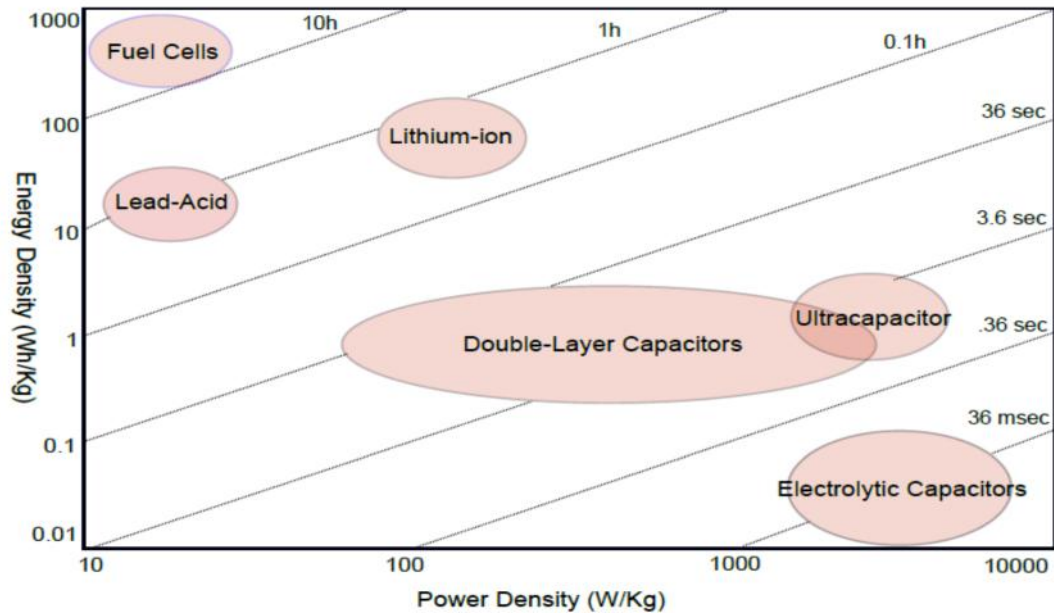


**Figure 2.4** Ragone plot displaying the energy and power properties of various technologies.  
Source: [18].

### 2.2.2 Ultracapacitor Cell Construction

In general, most ultracapacitor cell construction geometries are cylindrically shaped. The cells are constructed from activated carbon particles, mixed with a binder and then deposited on aluminum foil as shown in Figures 2.5 and 2.6. The electrodes are wound into a jellyroll configuration very similar to an aluminum electrolytic capacitor. The electrodes have foil extensions that are then welded to the terminals to enable a current path to the outside of the capacitor.

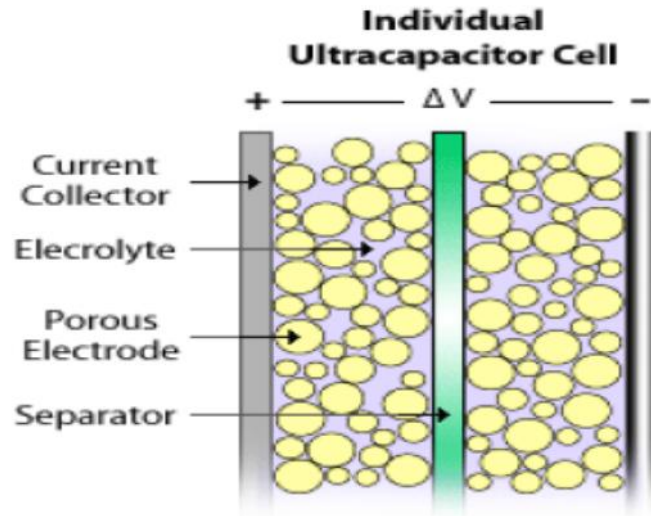


**Figure 2.5** Internal Cell Construction  
Source: [19].

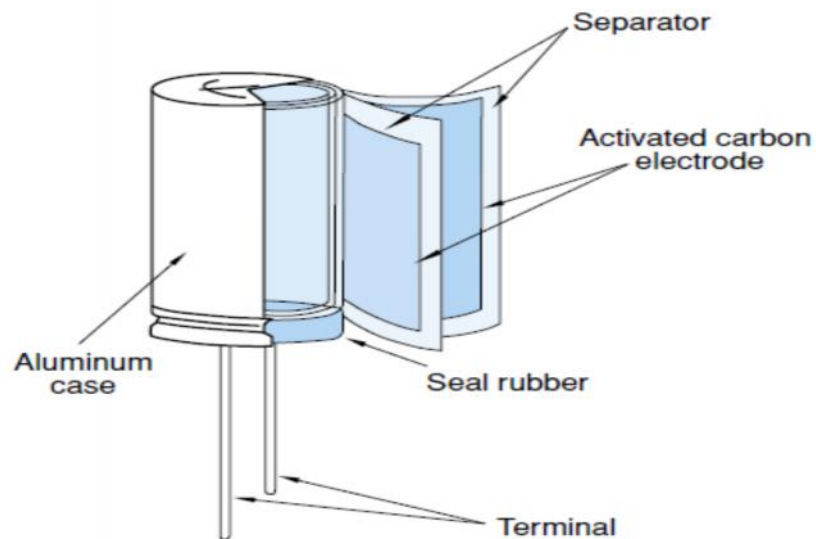


**Figure 2.6** Cell Construction  
Source: [19].

An ultracapacitor unit cell consists of two porous carbon electrodes (symmetric or asymmetric) that are isolated from electrical contact by a porous separator and are sealed in organic or aqueous electrolytes liquid [19]. Current collectors of metal foil or carbon impregnated polymers are used to conduct electrical current from each electrode. The

separator and the electrodes are impregnated with an electrolyte, which allows ionic current to flow between the electrodes while preventing electronic current from discharging the cell.

The configuration of ultracapacitor is shown in Figure 2.7. Consequently, in such a two terminal configuration, each electrode-electrolyte interface represents a capacitor so that the complete cell can be considered as two capacitors in series, as shown in Figure 2.7. The cell capacitance for the ultracapacitor cell can be calculated from:

$$C_{cell} = \frac{1}{\frac{1}{C_1} + \frac{1}{C_2}} \quad (2.5)$$

where,  $C_{cell}$  is the capacitance of the two-terminal device and  $C_1$  and  $C_2$  represent the capacitances of the two electrodes, respectively [20].

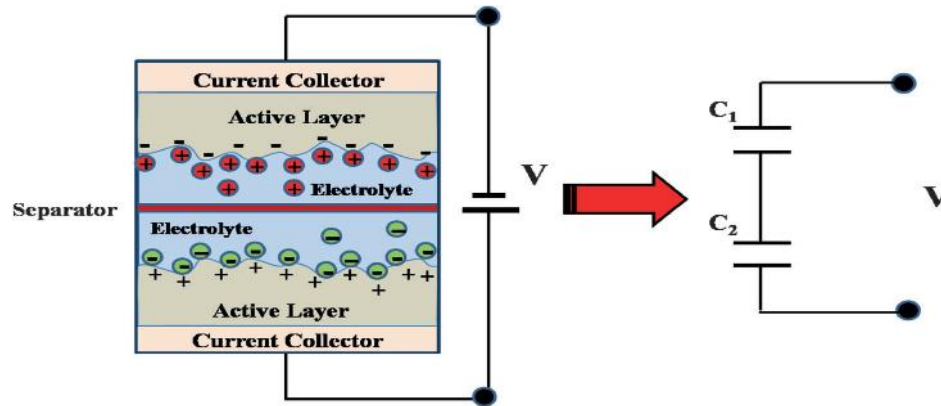


**Figure 2.7** Schematic representation of ultracapacitor cell.  
Source: [20].

### 2.2.3 Electrodes

In a traditional electrostatic capacitor, the electrodes consist of a thin surface on which the charges are gathered. For ultracapacitors, there are three main types of materials that are frequently used as ultracapacitor active electrode materials namely: (i) carbon

materials, e.g., carbon aerogel, activated carbon, carbon nanotubes and graphene; (ii) electroactive oxide or hydrous oxide films of transition metals, e.g.,  $\text{MnO}_2$ ,  $\text{RuO}_2$ ,  $\text{NiO}$ ,  $\text{Co}_3\text{O}_4$ ,  $\text{MoO}_3$ ; (iii) conducting polymers, example polypyrrole, polyaniline and polythiophene. Apart from symmetric electrodes (anode and cathode using the same electrode materials), some supercapacitors are designed based on asymmetrical electrode configurations (i.e., one electrode consists of electrostatic carbon material while the other consists of faradaic capacitance material). One obvious advantage of such asymmetric ultracapacitors is that both electric double-layer capacitance and faradaic capacitance mechanisms occur simultaneously, rendering a higher working voltage window and higher energy and power densities in ultracapacitors than with symmetric electrodes [20].

This structure of ultracapacitor electrode, gives a significantly larger specific surface area than the electrostatic (conventional) capacitors.

#### **2.2.4 Electrolyte**

The performance characteristics of ultracapacitors can be adjusted by changing the nature of its electrolyte. The electrolyte is also a critical factor that influences ultracapacitor performance. The main difference between ultracapacitor and conventional capacitor is that the electrolyte in the ultracapacitor contains free charges in the form of ions. The ordinary capacitor does not have this type of free charges.

The requirements for a good electrolyte include a wide voltage window, high electrochemical stability, high ionic concentration and low solvated ionic radius, low resistivity (ESR), low viscosity, low volatility, low toxicity, low cost, and availability at high purity [6,20]. Ultracapacitor can utilize either an aqueous or organic electrolyte.

There are two main commercial electrolytes today on the market, organic and aqueous [20]. Aqueous electrolytes, such as  $\text{H}_2\text{SO}_4$  and  $\text{KOH}$ , generally have lower ESR and lower minimum pore size requirements compared to organic electrolytes, such as acetonitrile (ACN). However, aqueous electrolytes also have lower breakdown voltages. Therefore, in choosing between an aqueous or organic electrolyte, one must consider the tradeoffs between capacitance, ESR, and voltage [6]. Because of these tradeoffs, the choice of electrolyte often depends on the intended application of the ultracapacitor.

The properties of the electrolyte set the rated voltage for the capacitors. The rated voltage must be lower than the oxidation voltage for the electrolyte. If the oxidation voltage is reached, a chemical process is started in the electrolyte that creates gases from the electrolyte. Today, electrolytes that are available give a rated voltage of up to 2.8 V. One important property of the electrolyte is that it must be able to dissolve some types of salt which provide the free ions in the capacitor. Another desired property is that the ions have a high mobility in the electrolyte. This is because the mobility mostly determines the series resistance of the ultracapacitor. High mobility gives low series resistance and vice versa. A third important property can be added to the electrolyte. This property is the temperature stability of the ion mobility. This property differs between the two electrolytes (aqueous and organic) that are used today. The ACN electrolyte gives a more stable series resistance during temperature changes compared to aqueous (PC), especially at low temperatures. The drawback of using ACN is that this substance has an environmental disadvantage. If the capacitor is over charged to the oxidation voltage, the resulting gases contain cyanide which is a toxic substance and, for this reason, it is not allowed to be used in some nations [7, 11].

### **2.2.5 Ultracapacitor Charge Separation**

Generally, capacitors are constructed with a dielectric placed between opposite electrodes, functioning as capacitors by accumulating charges in the dielectric material. In a conventional capacitor, energy is stored by the removal of charge carriers, typically electrons from one metal plate and depositing them on another. This charge separation creates a potential between the two plates, which can be harnessed in an external circuit. The total energy stored in this fashion is a combination of the number of charges stored and the potential between the plates. The former is essentially a function of size and the material properties of the plates, while the latter is limited by the dielectric breakdown between the plates. Various materials can be inserted between the plates to allow higher voltages to be stored, leading to higher energy densities for any given size.

In contrast, ultracapacitors do not have any dielectrics in general, but rather utilize the phenomena typically referred to as the electric double layer. In the double layer, the effective thickness of the “dielectric” is exceedingly thin as in Figure 2.7, and because of the porous nature of the carbon, the surface area is extremely high according to equation (2.2), which translates to a very high capacitance. Inside the ultracapacitor, there are mainly two physical laws that determine the behavior of the ions; diffusion and electrostatic relation. When the ultracapacitor has been completely discharged, the ions in the electrolyte become evenly distributed due to the diffusion as shown in Figure 2.8 [8]. As soon as the ultracapacitor is charged, the ions are attracted by the electric field which is formed between the electrodes. Because of this field, a separation of ions is started. The self-discharge of the ultracapacitor is mainly caused by the diffusion [4, 7, 21].

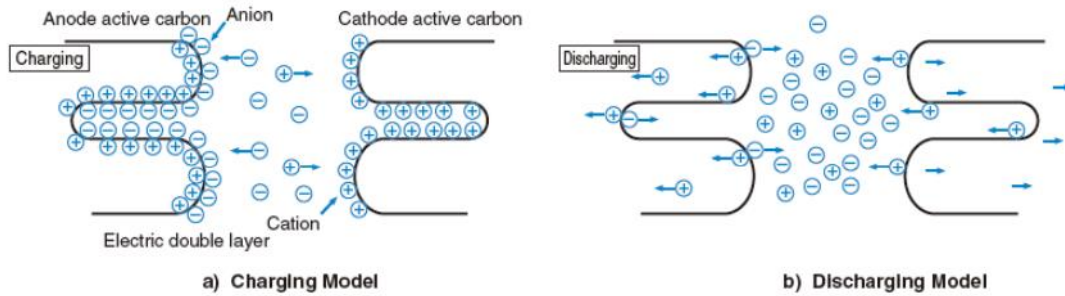


**Figure 2.8** Ultracapacitor Charge Separations

Source: [19].

However, the double layer capacitor can only withstand low voltages (typically less than 2.7V per cell), which means that electric double-layer capacitors rated for higher voltages must be made of matched series-connected individual capacitors, much like series-connected cells in higher-voltage batteries. Each product has its own advantages and disadvantages compared to other technologies as shown in Table 2.1 below:

**Table 2.1** Ultracapacitor vs. Battery and Conventional Capacitors [19]

Available Performance	Lead Acid Battery	Ultracapacitor	Conventional Capacitor
Charge Time	1 to 5 hrs	0.3 to 30 s	$10^{-3}$ to $10^{-6}$ s
Discharge Time	0.3 to 3 hrs	0.3 to 30 s	$10^{-3}$ to $10^{-6}$ s
Energy (Wh/kg)	10 to 100	1 to 10	<0.1
Cycle Life	1000	>500,000	>500,000
Specific Power (W/kg)	<1000	<10,000	<100,000
Charge/Discharge Efficiency	0.7 to 0.85	0.85 to 0.98	>0.95
Operating Temperature	-20 to 100 C	-40 to 65 C	-20 to 65 C

## 2.3 Classifications of Ultracapacitors

Ultracapacitors are characterized by their means of storing energy. Ultracapacitors can be divided into three general classes namely: Electrochemical double-layer capacitors, Pseudocapacitors, and Hybrid capacitors. Electrochemical double-layer capacitors store charges by Non-Faradaic process, Pseudocapacitors also store charges by Faradaic process while Hybrid capacitors store charges by combination of the two processes. Faradaic processes, such as oxidation-reduction reactions, involve the transfer of charge between electrode and electrolyte. A non-Faradaic mechanism, by contrast, does not use a chemical mechanism. Rather, charges are distributed on surfaces by physical processes that do not involve the making or breaking of chemical bonds.

This section will present an overview of each of these three classes of ultracapacitors and their subclasses, distinguished by electrode material. A graphical hierarchy of the different classes and subclasses of ultracapacitors are presented in Figure 2.9.

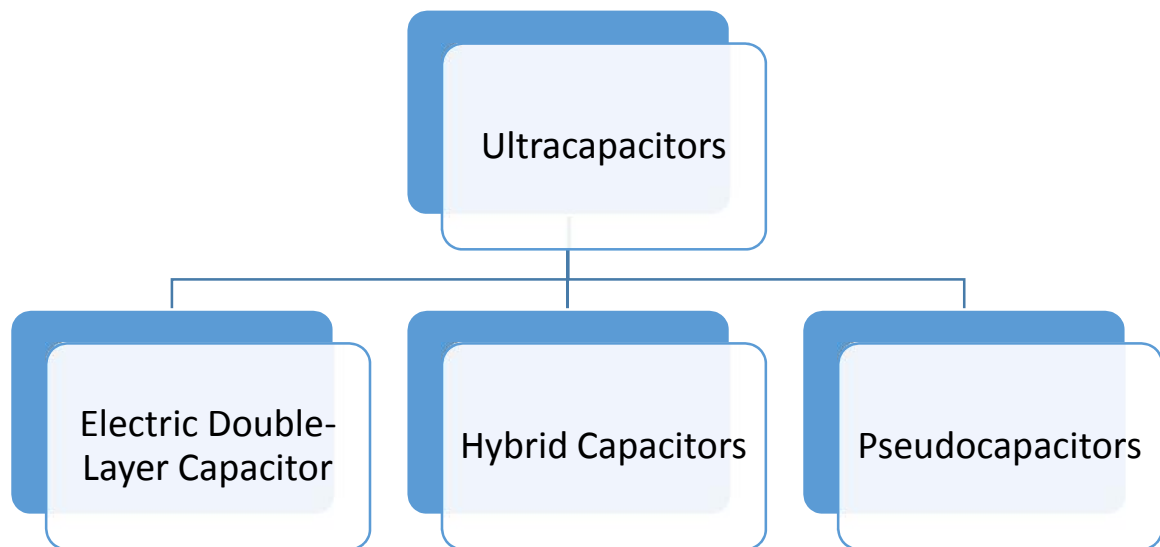


**Figure 2.9** Hierarchy of Ultracapacitors

### **2.3.1 Electrochemical Double-Layer Capacitors**

Electrochemical double-layer capacitors (EDLCs) are constructed from two carbon-based electrodes, an electrolyte, and a separator. Figure 2.2 provides a schematic of a typical EDLC. Like conventional capacitors, EDLCs store charge electrostatically, or non-Faradaically, and there is no transfer of charge between electrode and electrolyte.

EDLCs utilize an electrochemical double-layer of charge to store energy. As voltage is applied, charge accumulates on the electrode surfaces. Following the natural attraction of unlike charges, ions in the electrolyte solution diffuse across the separator into the pores of the electrode of opposite charge. However, the electrodes are engineered to prevent the recombination of the ions. Thus, a double-layer of charge is produced at each electrode as in Figure 2.2. These double-layers, coupled with an increase in surface area and a decrease in the distance between electrodes, allow EDLCs to achieve higher energy densities than conventional capacitors [3, 6, 15]. Because there is no transfer of charge between electrolyte and electrode, there are no chemical or compositional changes associated with non-Faradaic processes. For this reason, charge storage in EDLCs is highly reversible, which allows them to achieve very high cycling stabilities. EDLCs generally operate with stable performance characteristics for a great many charge-discharge cycles, sometimes as many as 10<sup>6</sup> cycles. On the other hand, electrochemical batteries are generally limited to only about 10<sup>3</sup> cycles. Because of their cycling stability, EDLCs are well suited for applications that involve non-user serviceable locations, such as deep sea or mountain environments [3, 6].

### **2.3.2 Pseudocapacitors**

In contrast to EDLCs, which store charge electrostatically, pseudocapacitors store charge Faradaically through transfer of charge between electrode and electrolyte. This is accomplished through electrosorption, oxidation - reduction reactions, and intercalation processes. These Faradaic processes may allow pseudocapacitors to achieve greater capacitances and energy densities than EDLCs [6]. There are two electrode materials that are used to store charge in pseudocapacitors, conducting polymers and metal oxides.

### **2.3.3 Hybrid Capacitors**

Hybrid capacitors attempt to exploit the relative advantages and mitigate the relative disadvantages of EDLCs and Pseudocapacitors to realize better performance characteristics [6]. Utilizing both Faradaic and non-Faradaic processes to store charge, hybrid capacitors have achieved energy and power densities greater than EDLCs without the sacrifices in cycling stability and affordability that have limited the success of Pseudocapacitors. This research has focused on three different types of hybrid capacitors, distinguished by their electrode configuration: composite, asymmetric, and battery-type respectively.

## **CHAPTER 3**

### **FUNDAMENTALS OF GRAPHENE-BASED ULTRACAPACITORS**

#### **3.1 Introduction**

In this chapter, fundamentals of graphene-based ultracapacitor electrode materials will be discussed. The objective is to present other competing material candidates for ultracapacitor cell design, fabrication techniques used in ultracapacitor electrode design, mechanical, thermal and electrical properties of graphene as applied to ultracapacitor cell design and Joule heating effects in ultracapacitor cell.

#### **3.2 Material Candidates for Ultracapacitor Electrodes**

The goal of ultracapacitor devices is to improve their performance in a limited footprint area by using high-capacitance active materials and well-designed 3D structures. Efforts to increase the energy and power densities by designing novel 3D structures for the electrodes have appeared in recent years [15,17], and various nano-structured materials have been used in the ultracapacitor electrodes. As in conventional capacitors, ultracapacitors are usually fabricated from three main types of materials: (i) carbon materials with high specific surface area, (ii) conducting polymers and (iii) metal oxides with high pseudocapacitance. In Section 3.2.1, the summary and analysis of the recent development in electrode materials and structures (particularly based on graphene), as well as the electrochemical performance of ultracapacitors, are presented.

### **3.2.1 Carbon Materials as non-Faradaic Electrodes**

Because of the advantages of low cost, easy processing, non-toxicity, high specific surface area, good electronic conductivity, high chemical stability, and wide operating temperature range, carbon materials are promising candidates for large-scale fabrication. To enable their use as ultracapacitor electrode materials, they must have the following properties [6, 15]: (i) high specific surface areas, of the order of  $1000 \text{ m}^2/\text{g}$ , (ii) good intra- and inter-particle conductivity in porous matrices, and (iii) good electrolyte accessibility to intra-pore regions. Carbon-based electrochemical capacitors function similarly to electrochemical double-layer capacitors, which rely on high specific area to accumulate non-faradaic charges at the boundary between an electrode and an electrolyte. Thus, unlike pseudocapacitive materials, carbon-based active materials exhibit true capacitive behavior and excellent chemical stability upon cycling [9]. To date, carbon materials with high specific areas such as carbon nanotubes, graphene, activated carbon, and carbon aerogels have been reported as active electrode materials in ultracapacitor cell design. Table 3.1 summarizes the reported electrochemical performance of the ultracapacitors based on these materials and is provided at the end of this Section 3.2.1.

**3.2.1.1 Activated Carbons as Electrode.** Activated carbons, produced by either thermal activation or chemical activation, are the most widely used electrode materials in EDLCs because they have a high specific surface area (approximately  $1200 \text{ m}^2/\text{g}$ ), good electrochemical stability, and a relatively high electronic conductivity in aqueous and organic electrolytes. Activated carbons utilize a complex porous structure composed of

differently sized micropores ( $< 20 \text{ \AA}$  wide), mesopores ( $20 - 500 \text{ \AA}$ ), and macropores ( $>500 \text{ \AA}$ ) to achieve their high surface areas [21].

Although capacitance is directly proportional to surface area, empirical evidence suggests that, for activated carbons, not all of the high surface area contributes to the capacitance of the device [6]. This discrepancy is believed to be caused by electrolyte ions that are too large to diffuse into smaller micro-pores, thus preventing some pores from contributing to charge storage. Although activated carbons are good candidates for ultracapacitor electrode materials, their specific capacitance might be further improved by adding pseudocapacitive materials like their more conventional counterparts.

**3.2.1.2 Carbon Aerogels as Electrodes.** There is also an interest in using carbon aerogels as an electrode material for ultracapacitors. Carbon aerogels are formed from a continuous network of conductive carbon nanoparticles with interspersed mesopores. Due to this continuous structure and their ability to bond chemically to the current collector, carbon aerogels do not require the application of an additional adhesive binding agents. As a binderless electrode, carbon aerogels have been shown to have a lower ESR than activated carbons [6,19,21]. This reduced ESR, which yields higher power, according to Equation 2.4, is the primary area of interest in ultracapacitor research involving carbon aerogels.

**3.2.1.3 Carbon Nanotubes (CNT) as Electrodes.** CNTs have attracted interest as electrode materials for ultracapacitors because of their unique structure, high surface area, low mass density, outstanding chemical stability and excellent electronic

conductivity. Compared with activated carbons, CNTs have several advantages: (i) the electrical conductivity of CNTs is greater than 100 S/cm, higher than activated carbon (2.5 S/cm); (ii) CNT electrodes are binder free and each tube is connected directly to the substrate, assuming that CNT arrays are grown by Chemical Vapor Deposition (CVD) and not dispersed onto the substrate from a liquid suspension, while activated carbon electrodes contain binder that increases the contact resistance between particles; (iii) most of the open space in CNT electrodes consist of mesopores that contribute to double-layer capacitance and fast ion transport rates [21], whereas the pore distribution of activated carbons contains a mixture of micropores (<2 nm), mesopores (2 to 50 nm), and macropores (>50 nm). Micropores can significantly increase the surface area but fail to produce the effect of double-layer capacitance due to the impedance of ion diffusion and ion-sieving effects, particularly when larger organic electrolytes are used.

To date, few studies of CNT-based ultracapacitor electrodes have been reported. Microelectrodes based on vertically aligned CNT arrays seem better than randomly aligned CNTs because random tubes might extend into the gap region between two adjacent electrodes to produce a short circuit. The reported capacitance of as-prepared CNT ultracapacitors was 36.5 F/g, with a calculated energy density of approx. 0.4 Wh/kg and a power density of approx. 1 kW/kg.

A common problem with CNT arrays as electrodes is associated with poor substrate bonding that is exposed when they are wetted by an aqueous electrolyte to cause not only detachment of CNTs from the substrate but also degradation of the vertical orientation resulting in poor cyclic stability. New fabrication techniques are needed to

achieve highly ordered CNT array electrodes that are optimized for CNT ultracapacitor applications.

**3.2.1.4 Graphene as Electrodes.** Since a mechanically exfoliated graphene monolayer was first observed and characterized in 2004 [21], much research in both scientific and engineering applications of graphene has been carried out worldwide, including extensive attempts to use graphene in ultracapacitors. Among the graphene materials, reduced graphene oxide (rGO) is most frequently used as an active material in ultracapacitors because of its low-cost, scalability, wet-chemical properties and the high density of chemically active defect sites [21], rGO is also of high interest in the fabrication of ultracapacitor electrodes. Interestingly, when a substantial amount of water is entrapped in the layered GO, it becomes a strongly anisotropic ion conductor as well as an electrical insulator, making it both a viable electrolyte and an electrode separator [21].

**Table 3.1** Summary of carbon-based ultracapacitors reported in contemporary literature [21]

Electrode (thickness)	Electrolyte	Capacitance (mF/cm <sup>2</sup> )	Capacitance cycle stability	Energy density	Power density	Ref.
Activated carbon (5 μm) [a]	1 M Et <sub>4</sub> NBF <sub>4</sub> in PC	11.6	-	10 mWh/cm <sup>3</sup>	~40 W/cm <sup>3</sup> [d]	[26]
Activated carbon (1–2 μm) [a]	1 M Et <sub>4</sub> NBF <sub>4</sub> in PC	2.1	-	1.8 μWh/cm <sup>2</sup>	44.9 mW/cm <sup>2</sup>	[84]
Activated carbon (50–70 μm) [a]	1 M NaNO <sub>3</sub>	90.7	-	-	51.5 mW/cm <sup>2</sup>	[78]
Activated carbon (336 μm) [a]	1 M Et <sub>4</sub> NBF <sub>4</sub> in PC	81	-	71.4 μWh/cm <sup>2</sup>	34.4 mW/cm <sup>2</sup>	[70]
Photoresist-derived carbon (115–140 μm) [a]	0.5 M H <sub>2</sub> SO <sub>4</sub>	75	12.3 % loss after 1000 cycles	-	-	[92]
CNT arrays (80 μm) [a]	Ionic liquid BMIM-PF <sub>6</sub>	0.428	No capacitance loss after 10 cycles	-	-	[108]
CNT array (34 μm) [a]	0.1 M NaSO <sub>4</sub>	36.5 F/g	-	-0.4 Wh/kg [d]	~1 kW/kg [d]	[82]
Reduced GO (22 μm) [a]	Water-entrapped GO	0.51	30 % loss after 10 000 cycles	0.43 mWh/cm <sup>3</sup>	1.7 W/cm <sup>3</sup>	[83]
Reduced GO (22 μm) [b]	Water-entrapped GO	~0.25	35 % loss after 10 000 cycles	0.19 mWh/cm <sup>3</sup>	9.4 W/cm <sup>3</sup>	[83]
1–2 layer graphene [a]	PVA/H <sub>3</sub> PO <sub>4</sub> polymer gel	0.08	-	2.8 nWh/cm <sup>2</sup>	2 μW/cm <sup>2</sup>	[66]
Reduced GO film (10 nm) [a]	PVA/H <sub>3</sub> PO <sub>4</sub> polymer gel	0.394	No capacitance loss after 1500 cycles	14 nWh/cm <sup>2</sup>	9 μW/cm <sup>2</sup>	[66]
Reduced GO (7.6 μm) [a]	PVA/H <sub>2</sub> SO <sub>4</sub> polymer gel	2.3	3 % loss after 1000 cycles	0.3 mWh/cm <sup>3</sup> [d]	70 W/cm <sup>3</sup> [d]	[41]
Reduced GO (7.6 μm) [a]	FS-IL Ionogels	1.79 [c]	No capacitance loss after 30 000 cycles	1 mWh/cm <sup>3</sup> [d]	200 W/cm <sup>3</sup>	[41]
Reduced GO/CNTs (6 μm) [a]	3 M KCl	6.1	little capacitance loss after 1000 cycles	0.68 mWh/cm <sup>3</sup>	~2.5 W/cm <sup>3</sup> [d]	[120]
Graphene/CNTs (20 μm) [a]	1 M Na <sub>2</sub> SO <sub>4</sub>	2.16	-	0.16 mWh/cm <sup>3</sup>	115 W/cm <sup>3</sup>	[121]
Graphene/CNTs (20 μm) [a]	1-Butyl-3-methylimidazolium tetrafluoroborate	3.93	1.6 % capacitance loss after 8000 cycles	2.42 mW/cm <sup>3</sup>	135 Wh/cm <sup>3</sup>	[121]
Carbide-derived carbon (50 μm) [b]	1 M H <sub>2</sub> SO <sub>4</sub>	~450 [c]	-	-	-	[74]
Carbide-derived carbon (50 μm) [b]	1 M TEABF <sub>4</sub>	~300 [c]	-	-	-	[74]
Onion-like carbon (7 μm) [a]	1 M Et <sub>4</sub> NBF <sub>4</sub> in PC	1.7	almost no loss after 10 000 cycles	~2 mWh/cm <sup>3</sup> [d]	1000 W/cm <sup>3</sup>	[26]
Mesocarbon microbead (100 μm) [b]	Solid-state [BMIM][BF <sub>4</sub> ]	100	47 % loss after 8000 cycles	10 μWh/cm <sup>2</sup>	0.575 mW/cm <sup>2</sup>	[125]
Super P carbon black (unknown thickness) [b]	1.5 M H <sub>2</sub> SO <sub>4</sub>	~0.8	-	-	-	[75]

[a] In-plane type. [b] Sandwich type. [c] Estimated from the given information in the literature. [d] Estimated from Ragone plots in the literature.

### **3.2.2 Pseudocapacitive Materials as Faradic Electrodes**

Electric double-layer capacitors that rely on physical ion adsorption at the boundary between electrode and electrolyte will only give limited capacitance, typically in the range of 10–50 mF/cm<sup>2</sup> [6, 15-16, 21]. Pseudocapacitance, however, may be 10–100 times larger because of Faradaic charge transfer. Consequently, ultracapacitors based on pseudocapacitive materials further increase energy and power densities. If they additionally maintain a good cyclic stability, they are highly desirable. The charge stored in such ultracapacitors includes both non-faradaic charge in the double-layer and Faradaic charge, as active pseudocapacitive materials undergo fast and reversible surface Redox reactions. To date, considerable effort has been devoted to developing electrode materials for ultracapacitors that exhibit pseudocapacitance. Among these pseudocapacitive materials are: conducting polymers and metal oxides, composite, asymmetric and Battery-Type electrodes.

In this section, a brief overview of Pseudocapacitive materials are discussed as well as the various pseudocapacitive materials for ultracapacitor electrode design.

#### **3.2.2.1 Metal Oxides**

Because of their high conductivity, metal oxides have also been explored as a possible electrode material for Pseudocapacitors. The majority of relevant research concerns Ruthenium oxide, RuO<sub>2</sub>. This is because other metal oxides have yet to obtain comparable capacitances. The capacitance of Ruthenium oxide is achieved through the insertion and removal, or intercalation, of protons into its amorphous structure. In its hydrous form (RuO<sub>2</sub>·xH<sub>2</sub>O), RuO<sub>2</sub> has been found to be an excellent material for ultracapacitor

applications and hence the capacitance exceeds that of carbon-based and conducting polymer materials [6, 21].

Furthermore, the ESR of hydrous Ruthenium oxide is lower than that of other electrode materials. As a result, Ruthenium oxide pseudocapacitors may be able to achieve higher energy and power densities than similar EDLCs and conducting polymer pseudocapacitors. However, Faradaic reactions are confined to the outermost layer such that a large portion of underlying  $\text{RuO}_2 \cdot x\text{H}_2\text{O}$  remains unreacted. Also, despite this potential, Ruthenium-based electrodes are expensive and suffer from a diminished high-rate capability. Thus, a major area of research is the development of fabrication methods and composite materials to reduce the cost of Ruthenium oxide, without reducing the performance.

**3.2.2.2 Conducting Polymers.** Conducting polymers have a relatively high capacitance and conductivity plus, a relatively low ESR and cost compared to carbon-based electrode materials [6]. Conducting polymer-based ultracapacitors predominately focus on electrochemically coating conducting polymers on metal current collectors, pre-patterned by conventional lithography techniques. In particular, the n/p-type polymer configuration, with one negatively charged (n-doped) and one positively charged (p-doped) conducting polymer electrode, has the greatest potential energy and power densities; however, lack of efficient n-doped conducting polymer materials has prevented these pseudocapacitors from reaching their potential.

The main limitations of conducting polymer-based ultracapacitors seem to be their poor cyclic stabilities, high self-discharge rates, low capacities due to the suboptimal doping, and limited mass transport within thick polymer layers.

Additionally, it is believed that the mechanical stress on conducting polymers during reduction-oxidation reactions limits the stability of these pseudocapacitors through many charge-discharge cycles. This reduced cycling stability has hindered the development of conducting polymer pseudocapacitors. One possible solution to these issues is to coat a thin layer of conducting polymer on a conducting template with a large specific area. Consequently, coating of conducting polymers on templates (e.g., graphene) might be an effective way to enhance the electrochemical performance of ultracapacitors.

**3.2.2.3 Composites.** Composite electrodes integrate carbon-based materials with either conducting polymer or metal oxide materials and incorporate both physical and chemical charge storage mechanisms together in a single electrode. The carbon-based materials facilitate a capacitive double-layer of charge and also provide a high-surface-area backbone that increases the contact between the deposited pseudocapacitive materials and electrolyte [6, 20].

Composite electrodes constructed from carbon nanotubes and polypyrrole, conducting polymers, have been particularly successful. Several experiments have demonstrated that this electrode is able to achieve higher capacitances than either a pure carbon nanotube or pure polypyrrole polymer-based electrode [21]. This is attributed to the accessibility of the entangled mat structure, which allows a uniform coating of

polypyrrole and a three-dimensional distribution of charge. Moreover, the structural integrity of the entangled mat has been shown to limit the mechanical stress caused by the insertion and removal of ions in the deposited polypyrrole. Therefore, unlike conducting polymers, these composites have been able to achieve a cycling stability comparable to that of EDLCs [6].

**3.2.2.4 Asymmetric.** Asymmetric hybrids combine Faradaic and non-Faradaic processes by coupling an EDLC electrode with a pseudocapacitor electrode. In particular, the coupling of an activated carbon negative electrode with a conducting polymer positive electrode has received a great deal of attention [6]. As discussed in Section 3.2.1, the lack of an efficient, negatively charged, conducting polymer material has limited the success of conducting polymer pseudocapacitors. The implementation of a negatively charged, activated carbon electrode attempts to circumvent this problem. While conducting polymer electrodes generally have higher capacitances and lower resistances than activated carbon electrodes, they also have lower maximum voltages and less cycling stability. Asymmetric hybrid capacitors that couple these two electrodes mitigate the extent of this tradeoff to achieve higher energy and power densities than comparable EDLCs. Also, they have better cycling stability than comparable pseudocapacitors [6].

#### **3.2.2.5 Battery-Type**

Like asymmetric hybrids, battery-type hybrids couple two different electrodes; however, battery-type hybrids are unique in coupling an ultracapacitor electrode with a battery electrode. This specialized configuration reflects the demand for higher energy

ultracapacitors and higher power batteries, combining the energy characteristics of batteries with the power, cycle life, and recharging times of ultracapacitors. Recent research has focused primarily on using Nickel hydroxide, Lead dioxide, and LTO ( $\text{Li}_4\text{Ti}_5\text{O}_{12}$ ) as one electrode and activated carbon as the other. Although there is less experimental data on battery type hybrids than on other types of ultracapacitors, the data that is available suggests that these hybrids may be able to bridge the gap between ultracapacitors and batteries. Despite the promising results, the general consensus is that more research will be necessary to determine the full potential of Battery-type hybrids [6, 16]. Table 3.2 provides a summary of the ultracapacitor performance based on pseudocapacitive materials reported in the literature so far.

**Table 3.2** Summary of pseudocapacitive ultracapacitor performance [21]

Electrode (thickness)	Electrolyte	Capacitance ( $\text{mF}/\text{cm}^2$ )	Capacitance cycle stability	Energy density	Power density	Ref.
Hydrous $\text{RuO}_2$ (10 $\mu\text{m}$ ) [a]	0.5 M $\text{H}_2\text{SO}_4$	174 F/g	–	23 Wh/kg	96.5 W/kg	[160]
Hydrous $\text{RuO}_2$ (1.9 $\mu\text{m}$ ) [a]	0.5 M $\text{H}_2\text{SO}_4$	40.7	–	$-1.1 \mu\text{Wh}/\text{cm}^2$ [e]	$-0.4 \text{mW}/\text{cm}^2$ [e]	[135]
W- $\text{RuO}_2$ (1 $\mu\text{m}$ ) [b]	LiPON	54.2	–	–	–	[161]
$\text{MnO}_2/\text{CNT}$ array (34 $\mu\text{m}$ ) [a]	0.1 M $\text{NaSO}_4$	176 F/g	–	10.3 Wh/kg	960 W/kg	[82]
$\text{MnO}_2$ nanofiber (1 $\mu\text{m}$ ) [a]	Solid-state $\text{H}_3\text{PO}_4$ -PVA	341.4 F/g	4% loss after 500 cycles	–	–	[138]
PPy vs. PPy [a]	0.1 M $\text{H}_3\text{PO}_4$	$\sim 1.6$ – $14$ [c]	–	–	–	[141]
PPy vs. PPy [a]	0.5 M $\text{Et}_4\text{NBF}_4$ in ACN	$\sim 3.9$ [c]	–	–	–	[141]
PPy vs. PPT [a]	0.5 M $\text{Et}_4\text{NBF}_4$ in ACN	$\sim 5.2$ [c]	–	–	–	[141]
PPy on 3D Si (150 $\mu\text{m}$ ) [a]	1 M KCl	30	almost no loss after 800 cycles	–	–	[162]
PPy on 3D Si (150 $\mu\text{m}$ ) [a]	Solid-state $\text{LiClO}_4$ -PVA	29	–	–	$2.2 \text{mW}/\text{cm}^2$	[71]
PPy on 3D Si beams (unknown) [a]	0.5 M NaCl electrolytes	56	–	–	$0.56 \text{mW}/\text{cm}^2$	[72]
PPy/PR-derived carbon (140 $\mu\text{m}$ ) [a]	1 M KCl	78.35	44% loss after 1000 cycles	–	$0.63 \text{mW}/\text{cm}^2$	[93]
PANI nanowire (400 nm) [a]	Solid-state $\text{H}_2\text{SO}_4$ -PVA	$\sim 23.5$ [d]	4% loss after 1000 cycles	$2.9 \mu\text{Wh}/\text{cm}^2$ [d]	$50 \text{mW}/\text{cm}^2$ [d]	[142]
PANI nanorod/rGO (100–200 nm) [a]	Solid-state $\text{H}_3\text{PO}_4$ -PVA	970 F/g	10% loss after 1700 cycles	–	–	[153]

[a] In-plane type. [b] Sandwich type. [c] Estimated from the capacitance and effective device area in the literature. [d] Estimated from the specific volumetric capacitance and device dimension in the literature. [e] Estimated from the value and device dimension in the literature.

### **3.3 Fabrication Techniques for Graphene-Based Electrodes**

This section summarizes various techniques that have been used in the fabrication of ultracapacitors notably; Lithography-based technique, Inkjet printing technique, Femtosecond laser writing technique and Micro-molding in capillary (MIMIC) techniques.

#### **3.3.1 Lithography-Based Technique**

Progress in micro and nanofabrication techniques provides a scalable basis for fabricating ultracapacitor electrodes using conventional lithography-based techniques. These techniques are often selected when the patterned graphene-based materials are thin and require a precise separation between two adjacent electrodes. In order to pattern thick active materials as microelectrodes, selective etching of active materials is performed using metal masks patterned by conventional optical lithography techniques. In this case, the gap width between two adjacent electrodes can be easily adjusted by controlling the optical lithography parameters. As an example, 200-nm-thick electrodes of carbide-derived carbon films have been fabricated for ultracapacitors using patterned metal masks on top of the active materials [21]. However, this technique might not be applicable when the substrate surface is rough or porous (For example, free-standing porous CNT network). Effective etching methods to pattern active materials should also be taken into consideration. For instance, an impractically long time of oxygen plasma etching might be needed to pattern a 200-nm-thick graphite foil to fabricate microelectrodes.

### **3.3.2 Inkjet Printing Technique**

Inkjet printing technology has proven efficient when patterning liquid precursor materials such as structural polymers, conducting polymers, sol-gel materials, ceramics, nanoparticles, nucleic acid and protein arrays for the fabrication of electronic devices, sensors, and the functionalization of biomedical surfaces [21]. Inkjet printing offers the following advantages: (i) short processing time, (ii) low capital and production costs, (iii) applicability to non-planar substrates, (iv) ease in processing, particularly when compared to photolithographic techniques, and (v) an easy path to meet industrial scale-up needs. For these reasons, inkjet printing is considered to be simpler, more environmentally friendly and cost effective than vacuum-based methods [20, 21]. Inkjet printing has been successfully used to print conducting metal patterns from Ag, Pd, Au, Pt, Cu, and conducting polymers [21].

Various ultracapacitors were designed with this technique with interdigitated fingers ranging from 40 to 100  $\mu\text{m}$  width. However, common problems associated with inkjet methods include large drops of ink that preclude the ability to print fine interdigitated fingers, limited precision for narrow electrodes and gaps, and coalescence of drops affecting the print quality.

### **3.3.3 Femtosecond Laser Writing Technique**

Femtosecond lasers have been widely used for producing micron features and 3D microdevices in many fields due to their advantages of nanometer spatial resolution and 3D prototyping capability [21]. A direct femtosecond laser reduction process to make graphene-based electronic microcircuits on graphene oxide films has been demonstrated

[16, 21]. Free-standing and flexible ultracapacitors on a GO film were fabricated based on the laser writing techniques [11]. Laser writing has also been used to fabricate supercapacitors on a large scale by a standard LightScribe DVD burner [21]. A laser drive can write desired graphene circuits onto a GO film following computer-designed patterns. Various microdevices with different sizes and shapes can be produced on a single run. This method would be promising for large-scale fabrication of ultracapacitors if the cost of femtosecond laser equipment can be reduced.

### **3.3.4 Micro-Molding in Capillary (MIMIC) Technique**

Micro-molding in capillary (MIMIC) has been used to fabricate microstructures of organic polymers, inorganic and organic salts, ceramics, metals, and crystalline micro-particles in many different kinds of patterns. The technique relies on the spontaneous filling of channels with a fluid by capillary action, in which the rate and the extent of filling are determined by the balance between interfacial thermodynamics and viscosity drag [21]. The merits of this method in fabricating micro-pattern electrodes are as follows:

- fabrication of a mold in MIMIC is simple; it requires only the conformal contact of a substrate with an elastomeric mold;
- only limited (and in some cases no) access to facilities for lithography; and
- the production of multiple copies of an elastomeric component from a single lithographic master.

However, this method is limited to low-viscosity liquids. This liquid-based process can be an effective alternative to fabricate ultracapacitor electrodes. Large-scale

micro-patterns of continuously conductive rGO films that are centimeters in length and micrometers in width on various substrates were fabricated using the micro-molding and their capabilities in a sensing application were demonstrated in a recent study [21]. Ultracapacitors, based on rGO micro-patterns, fabricated by this method were reported recently [21].

### **3.4 Properties of Graphene-Based Electrodes**

#### **3.4.1 Mechanical Properties of Graphene**

Graphene, a monolayer of covalently bonded carbon atoms, represents a new two-dimensional (2D) material having the unique mechanical and transport properties that are desired for a wide range of technologies. In particular, graphene shows outstanding electron transport properties due to its 2D hexagonal crystal structure and the presence of charge carriers behaving like massless particles. In addition, graphene is specified by extremely high in-plane stiffness –Young’s modulus - and superior (highest ever measured) strength [2, 12]. The exceptional mechanical properties of graphene are of utmost importance for its applications, because they are highly needed (i) to exploit graphene as a super-strong structural material; (ii) to understand and control the durability of graphene used in electronics and energy storage; (iii) to plastically form curved graphene specimens for electronics and structural applications; (iv) to exploit nano composites with graphene inclusions as structural and/or functional materials.

The mechanical equivalent to Ohm’s law is Hooke’s law. For a material in one dimension, it is expressed as:

$$\sigma = E \varepsilon \quad (3.1)$$

where the stress  $\sigma$  is the force per unit area,  $E$  is the Young's modulus, and  $\varepsilon$  is strain.

This assumes an isotropic system where there is no preferred crystal orientation. In many bulk solids, this is a valid assumption considering that single crystals tend to be separated into grains of random orientation. When taken as a whole, the elastic constants average to some bulk value, [10]. Table 3.3 shows typical Young's modulus for various materials.

Most materials tend to contract in the direction perpendicular to the applied strain. The ratio of the strains in these two directions defines a quantity known as Poisson's ratio:

$$\nu = - \frac{\varepsilon_y}{\varepsilon_x} \quad (3.2)$$

Typical Poisson's ratios are shown in Figure 3.1. Some materials like the cork of a wine bottle have  $\nu \approx 0$  while others like rubber have  $\nu \approx 0.5$ . There also exists a class of exotic materials with  $\nu < 0$  (Figure. 3.1c).

Equations (3.1) and (3.2) can be combined to give the isotropic three dimensional version of Hooke's law which relates stress to strain as:

$$\varepsilon_{xx} = \frac{1}{E} ( \sigma_{xx} - \nu ( \sigma_{yy} + \sigma_{zz} ) ) \quad (3.3)$$

Biaxial strain is a common type of strain where both the x and z component of strain are equivalent:  $\varepsilon_x = \varepsilon_z = \varepsilon$ . An example is the surface of a spherical balloon where a pressure difference across the balloon applies an equal strain to both directions. For biaxial strain of an isotropic plate, the modified form of Hooke's law simplifies to:

$$\sigma = \frac{E}{1-\nu} \varepsilon \quad (3.4)$$

It should be noted that cubic crystals are biaxially isotropic along the (111) and (100) planes.

**Table 3.3** Approximate Young's modulus for various materials [2]

<b>Material</b>	<b>Young's Modulus (<math>E</math>) in GPa</b>
Rubber (small strain)	0.01-0.1
PTFE (Teflon)	0.5
Nylon	3-7
Oak wood (along grain)	11
High-strength concrete ( under compression)	30
Aluminum alloy	69
Glass ( see also diagram below table)	65-90
Titanium (Ti)	105-120
Copper (Cu)	110-130
Silicon (Si)	150
Wrought iron and steel	190-210
Tungsten (W)	400-410
Silicon carbide (SiC)	450
Diamond ( C )	1,050-1,200
Single walled carbon nanotube	1,000
Graphite/Graphene ( within the plane)	1,000

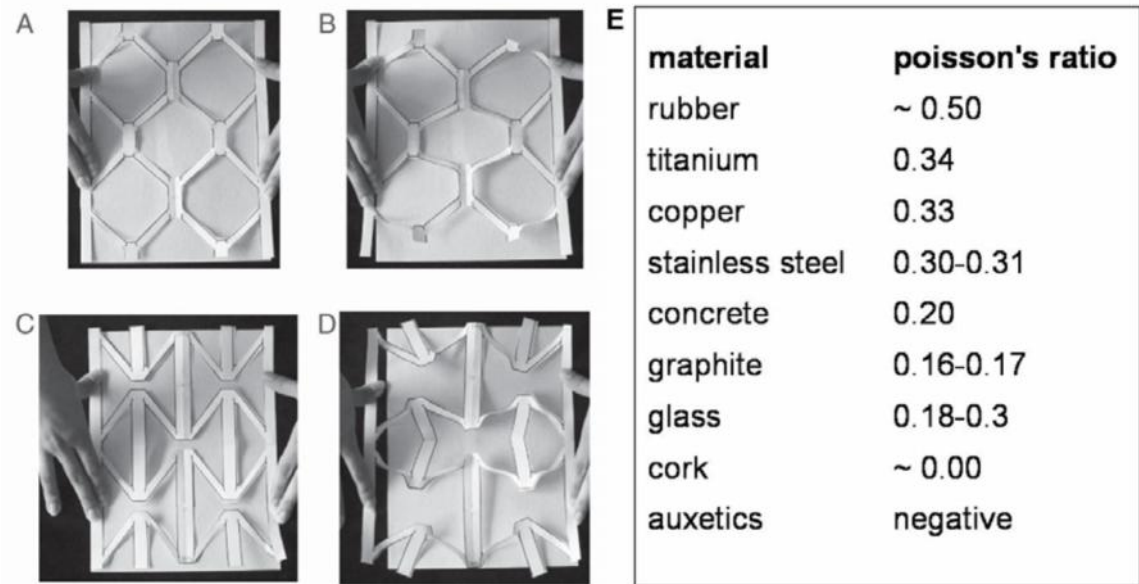


**Figure 3.1** Dpe (A) unstretched and (B) stretched. Lattice with a negative Poisson ratio: (C) unstretched and (D) stretched. The sheet of paper behind each figure has the same dimensions. Figure from (Campbell and Querns 2002) (E) A table of Poisson's ratio for common materials. Adapted from Wikipedia-Poisson's ratio. Source: [2].

Graphite is unique in that the elastic constants in the perpendicular direction are vastly different than the elastic constants along the basal plane.

The first careful attempts to determine the mechanical elastic constants measured the resonance frequency of cantilevers of natural graphite flakes. Cantilevers with length,  $L = 0.4 \text{ cm} - 1.0 \text{ cm}$  and thicknesses  $t =$  of  $0.01 \text{ cm} - 0.05 \text{ cm}$  were cut from natural graphite flakes. For vibrations dominated by shear, the resonance frequency,  $f$  is determined solely by the shear modulus  $G$ :

$$f = \frac{1}{2L} \sqrt{\frac{G}{\rho}} \quad (3.5)$$

where,  $\rho$  is the resistivity. By examining the length dependence, vibrations in as-received graphite samples were determined and were dominated by shear with a modulus,  $G = 0.1$  GPa while irradiated crystals were dominated by bending with  $E = 0.6$  TPa [11].

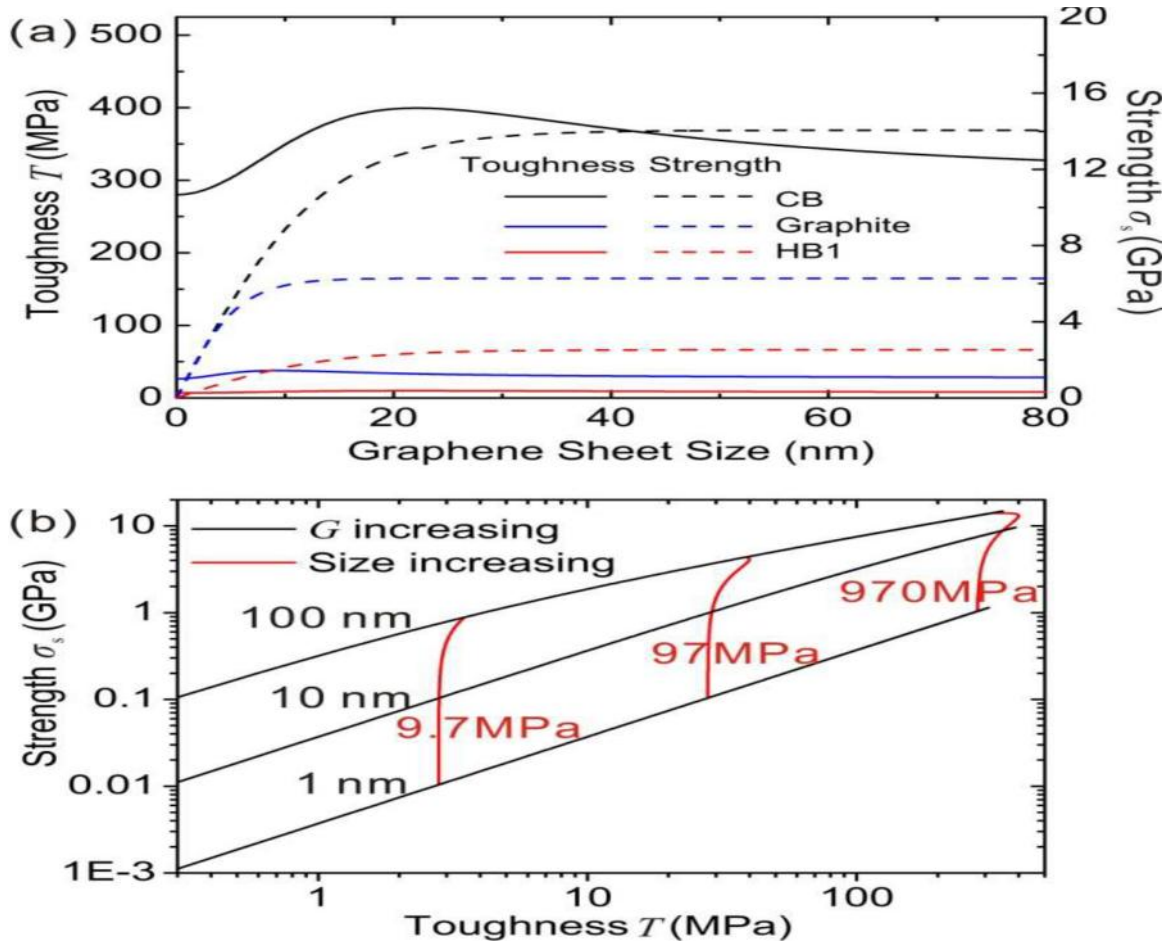


**Figure 3.2** (a) Dependences of strength and toughness of the two representative crosslink types (coordinative bonds, CB and hydrogen bonds between epoxy and hydroxyl groups, HB1) and graphite. (b) The dependence of tensile strength and toughness on interlayer shear modulus  $G$  and graphene sheet size  $l$ . Source: [2].

Furthermore, research suggests that varying the shear modulus and graphene sheet size, may have significant impact on the mechanical properties of the graphene papers – (Figure 3.2). Figure 3.2 (b) shows that the strength changes from 10 MPa to 10 GPa and toughness changes from 3 MPa to 400 MPa. Thus, by increasing the graphene sheet size

and crosslink strength, the strength and toughness of the materials will be enhanced cooperatively.

### 3.4.2 Thermal Properties

As mentioned above, most thermal properties of graphene are derived from those of graphite and bear the imprint of the highly anisotropic nature of this crystal. Graphene, as a two-dimensional (2D) material, has over 100-fold anisotropy of heat flow between the in-plane and out-of-plane directions. The high in-plane thermal conductivity is due to covalent  $sp^2$  bonding between carbon atoms, whereas out-of-plane heat flow is limited by weak van der Waals coupling.

In contrast, the strong and anisotropic bonding as well the low mass of the carbon atoms gives graphene and related materials unique thermal properties.

The thermal conductivity ( $\kappa$ ) of a material relates the heat flux per unit area,  $Q''$  (example in  $W/m^2$ ), to the temperature gradient,

$$Q'' = -\kappa \nabla T \quad (3.6)$$

The sign in this relationship is negative, indicating that heat flows from high to low temperature. The thermal conductivity can be related to the specific heat by;

$$\kappa = \Sigma C v \lambda \quad (3.7)$$

where,  $v$  and  $\lambda$  are the appropriately averaged phonon group velocity and mean free path, respectively. This expression is commonly used under diffusive transport conditions, when sample dimensions are much greater than the phonon mean free path ( $L \gg \lambda$ ).

The in-plane thermal conductivity of graphene at room temperature is among the highest of any known material, about  $2000\text{--}4000 \text{ Wm}^{-1} \text{ K}^{-1}$  for freely suspended samples

[13], as shown in Figure 3.3(a–b). The upper end of this range is achieved for isotopically purified samples (0.01%  $^{13}\text{C}$  instead of 1.1% natural abundance) with large grains, whereas the lower end corresponds to isotopically mixed samples or those with smaller grain sizes. Naturally, any additional disorder or even residue from sample fabrication will introduce more phonon scattering and lower these values further. For example, the thermal conductivity of natural diamond is  $\sim 2200 \text{ Wm}^{-1} \text{ K}^{-1}$  at room temperature [13] (that of isotopically purified diamond is 50% higher, or  $\sim 3300 \text{ Wm}^{-1} \text{ K}^{-1}$ ), and those of other related materials are plotted in Figure 3.3 (a–b). In particular, Figure 3.3 b shows presently known ranges of thermal conductivity at room temperature, with the implication that all lower bounds could be further reduced in more disordered samples.

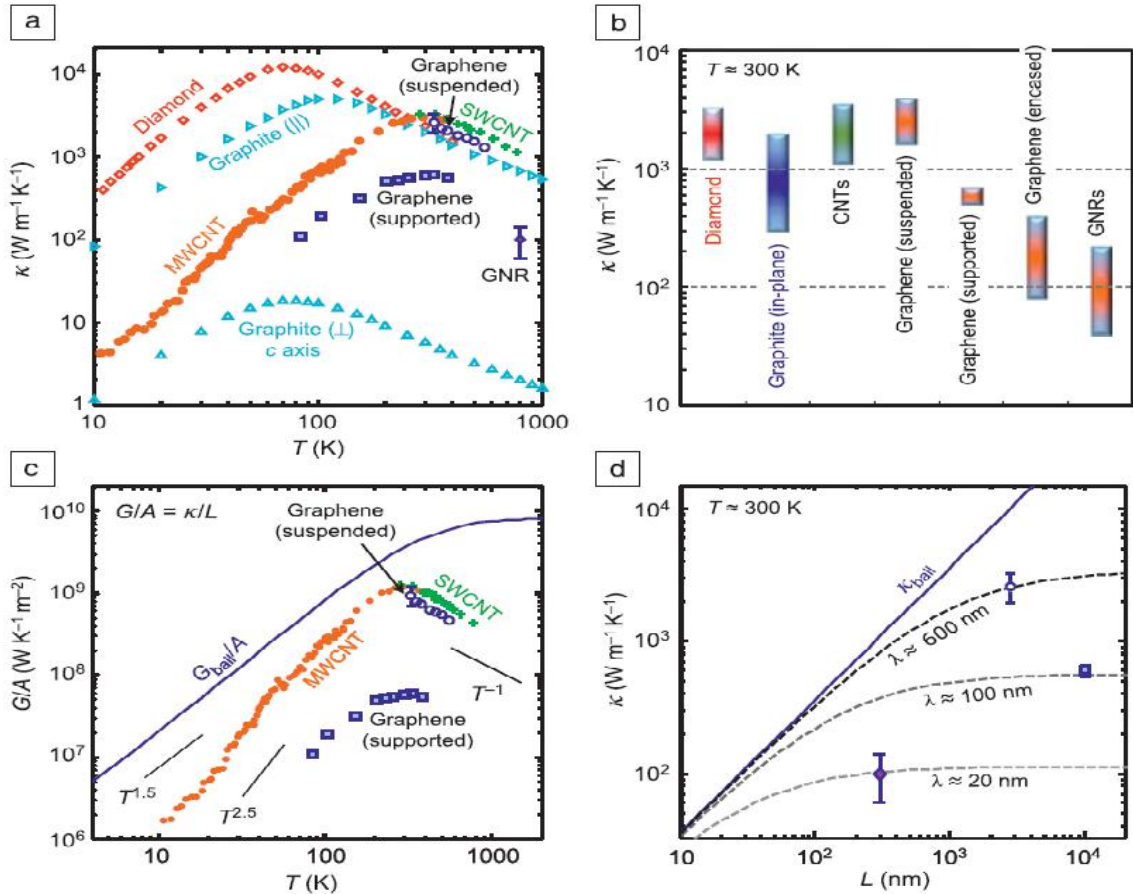


**Figure 3.3** (a) Thermal conductivity  $\kappa$  as a function of temperature: representative data for suspended graphene (open blue circles), SiO<sub>2</sub>-supported graphene (solid blue squares),  $\sim 20$ -nm-wide graphene nanoribbons (GNRs, solid magenta diamond), suspended single-walled carbon nanotubes (SWCNTs, green crosses), multiwalled CNTs (MWCNTs, solid orange circles), type IIa diamond (open red diamonds), graphite in-plane (sideways open blue triangles), and graphite out-of-plane (upright open blue triangles)

(b) Room-temperature ranges of thermal conductivity  $\kappa$  for diamond, graphite (in plane), Carbon nanotubes (CNTs), suspended graphene, SiO<sub>2</sub>-supported graphene, SiO<sub>2</sub>-encased graphene, and GNRs.

(c) In-plane thermal conductance  $G$  per unit cross sectional area  $A$  for graphene and related materials (symbols), compared to the theoretical ballistic limit,  $G_{ball}/A$  (solid line).

(d) Expected scaling of thermal conductivity  $\kappa$  with sample length  $L$  in the quasiballistic regime at  $T \approx 300$  K. The solid line is the ballistic limit,  $\kappa_{ball} = (G_{ball}/A)L$ , and dashed lines represent  $\kappa$  estimated with phonon mean free paths as labeled, chosen to match existing data for suspended graphene, supported graphene, and GNRs from top to bottom, respectively; symbols are consistent with panels (a) and (c).

Source: [13].

By contrast, heat flow in the cross-plane direction (along the  $c$  axis) of graphene and graphite is strongly limited by weak interplane Van der Waals interactions. The thermal conductivity along the  $c$  axis of pyrolytic graphite is a mere  $\sim 6 \text{ Wm}^{-1} \text{ K}^{-1}$  at room temperature, [13] as shown in Figure 3.3 a. Heat flow perpendicular to a graphene sheet is also limited by weak Van der Waals interactions with adjacent substrates, such as  $\text{SiO}_2$ . The relevant metric for heat flow across such interfaces is the thermal conductance per unit area, at room temperature. The heat flow given by;

$$G'' = \frac{Q''}{\Delta T} \approx 50 \text{ MWm}^{-2} \text{ K}^{-1} \quad (3.8)$$

and could become a limiting dissipation bottleneck in highly scaled graphene devices and interconnects [5, 13]. Interestingly, the thermal resistance,  $1/ G''$ , does not change significantly across few-layer graphene samples [13] (i.e., from one to 10 layers), indicating that the thermal resistance between graphene and its environment dominates that between individual graphene sheets. Indeed, the interlayer thermal conductance of bulk graphite is  $\sim 18 \text{ GW m}^{-2} \text{ K}^{-1}$  if the typical spacing (Figure 3.3a) and  $c$ - axis thermal conductivity are assumed.

### 3.4.3 Electrical Properties

When new material is discovered, the forces within the material are identified to immediately know two characteristics: how the electrons in the material respond to electrical forces and how the atoms respond to mechanical forces. The first of these is summed up by Ohm's Law:

$$V = IR \quad (3.9)$$

where  $V$  is the voltage difference across the conductor,  $I$  is the current, and  $R$  is the resistance. A useful way to express this resistance is in terms of a resistivity  $\rho$  defined as:

$$R = \frac{\rho}{A} L \quad (3.10)$$

where  $L$  is the length of the material and  $A$  is the cross sectional area through which the current is flowing. The resistivity of a material is independent of its geometry making it a useful quantity to compare different materials.

Ohm's law is a general formula applicable to 3D, 2D, and 1D conductors. In a typical conductor, charges are moving and scattering at random with no net movement of charge across the sample. This situation changes when a voltage difference,  $V$ , is applied across the conductor. The voltage difference creates an electric field,  $E$ , which gives these randomly scattered electrons a net force in one direction. Some of the possible scattering mechanisms are phonons in the material, defects in the lattice, or charge in homogeneities in the material. The velocity with which the charges move in the direction of the applied field is known as the drift velocity,  $V_d$  and is related to the current density  $J$  by:

$$J = nev_d \quad (3.11)$$

where  $n$  is the charge carrier density and  $e$  is the electron charge. When there is less scattering in a material, the charge carriers will travel farther with the same electric field.

This ratio is defined as the mobility,

$$\mu = \frac{V_d}{E} \quad (3.12)$$

and is an important quantity that is used to characterize scattering in conductors. One can then express the resistivity of a material in terms of its mobility by:

$$\rho = \frac{1}{(ne\mu)} \quad (3.13)$$

**3.4.3.1 Hall Effect.** In a magnetic field, a moving charge experiences a Lorentz force. Using the Drude model with an applied magnetic field  $B$ , the current density is defined as:

$$J = \frac{1}{\rho} \bar{E} - \frac{1}{ne} \bar{J} \times \bar{B} \quad (3.14)$$

which can be rewritten as:

$$\bar{E} = \rho \bar{J} + \frac{1}{ne} \bar{J} \times \bar{B} \quad (3.15)$$

We can then formulate this equation in matrix form using Cartesian coordinates and under the assumption that we have a 2D system with a B field in the z direction and current in the xy plane. Doing so we get:

$$\begin{matrix} E_x \\ E_y \end{matrix} = \begin{matrix} -\frac{\rho}{ne} & \frac{B}{\rho} \\ \frac{B}{ne} & \rho \end{matrix} \begin{matrix} J_x \\ J_y \end{matrix} \quad (3.16)$$

Referring to Figure 3.4, Hall resistance,  $R_H$ , can be defined as:

$$R_H = \frac{V_h}{I} \quad (3.17)$$

where:

$$V_h = E_y \cdot dl \quad (3.18)$$

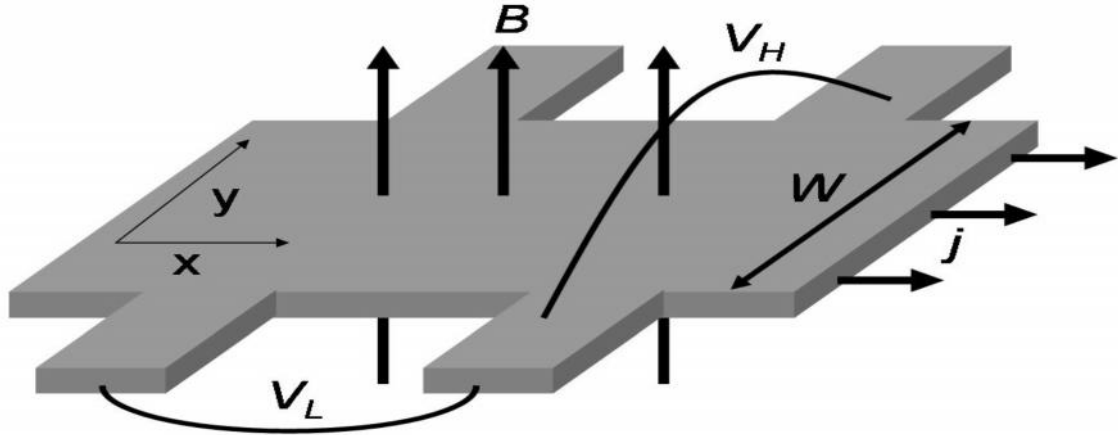


**Figure 3.4** Hall Bar geometry.

Source: [2].

With no current flow in the  $y$  direction, (3.14) simplifies to:

$$E_y = -\frac{B}{ne} j_x \quad (3.19)$$

Using (3.17) in (3.16), we get:

$$V_h = \int \frac{B}{ne} j_x dl = \frac{B}{ne} j_x W \quad (3.20)$$

In two dimensions, the current density is defined as:

$$j_x \equiv \frac{I}{W} \quad (3.21)$$

Using this fact along with the definition for the Hall voltage in (3.16), we have:

$$R_h = \frac{B}{ne} \quad (3.22)$$

By sweeping a perpendicular magnetic field,  $B$ , and measuring  $R_H$ , one can determine the carrier density,  $n$ . This density and the measured longitudinal resistivity  $\rho$  can be used to measure the sample's mobility  $\mu$ . This is a technique known as the Hall Effect and is commonly used to characterize conducting samples.

At low temperatures and high magnetic fields, the exceptional mobility of graphene allows for the observation of the quantum Hall effect for both electrons and holes (Figure 3.5b), [2]. Due to its unique band structure, the graphene quantum Hall Effect exhibits a subtle difference from the conventional quantum Hall effect in that plateaus occur at half integers of  $4e^2/h$  rather than the typical  $4e^2/h$ .

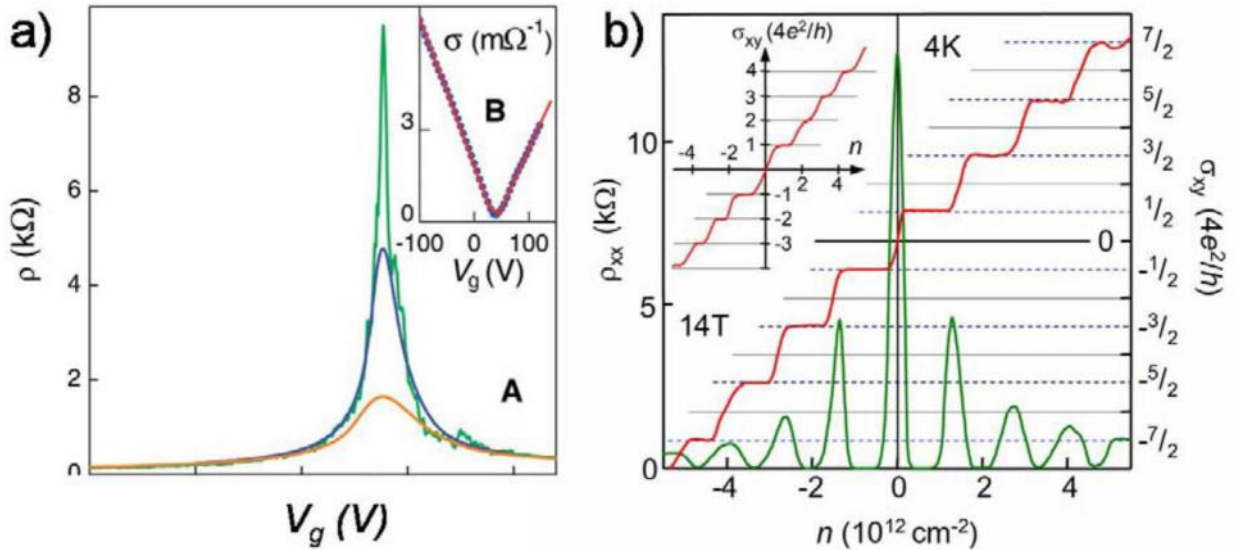


**Figure 3.5** a) The resistivity of a single layer of graphene vs. gate voltage. b) The Quantum Hall Effect in single layer graphene.

Source: [2].

### 3.5. Joule Heating Effects in Graphene-Based Ultracapacitors

As electrons gain energy from an external source (such as an electrical bias), a part of the excess energy is transferred to the lattice via phonon emission. Subsequent increase in the lattice temperature (i.e., the Joule heating) acts as a counter weight to limit further energy gain from the source by causing degradation in the electronic transport. Eventually, a balance is reached and the system approaches steady state. Thus, the details of heat dissipation including the properties of its primary path (i.e., the substrate) could have a

major influence. This is even more so in graphene-based structures, where the two-dimensional (2D) nature dictates a large interface with the substrate compared to the volume.

Experiments shows that the heat generation in an ultracapacitor cell consists of an irreversible Joule heating and a reversible heat caused by a change in entropy based on the analysis of the thermal measurement data obtained for an ultracapacitor [8,14]. The irreversible Joule heat generation rate (W),  $Q_J$ , is calculated by using the terminal current,  $I$ , of the ultracapacitor and the equivalent resistance,  $R_T$ , of three RC parallel branches as:

$$Q_J = I^2 R_T \quad (3.23)$$

The reversible heat generation rate (W),  $Q_R$ , is calculated by using the terminal current,  $I$ , of the ultracapacitor and the absolute temperature (K),  $T_{abs}$ , as:

$$Q_R = \alpha T_{abs} I \quad (3.24)$$

where,  $\alpha$  is a fitting parameter ( $V \cdot K^{-1}$ ). Although an explicit expression for  $Q_R$  was obtained, it contains parameters which are difficult to evaluate for porous electrodes and treating  $\alpha$  as a fitting parameter is a more practical approach. The value of  $\alpha$  is used to calculate reversible heat generation. Measured results suggest that the irreversible heat was caused by the Joule heat loss through the porous structure and the reversible heat by the ion adsorption on the carbon surface.

## **CHAPTER 4**

### **DEVICE MODELING, SIMULATION AND DISCUSSION**

#### **4.1 Introduction**

In the high pulse power operations for automotive applications, a large amount of heat is produced inside the ultracapacitor cell [8, 11]. Because the lifetime and performance of ultracapacitor depend strongly on temperature [1, 8], it is important to be able to accurately predict the electrical and thermal behaviors of ultracapacitor for its efficient and reliable system integration from an application perspective. Modeling of the electrical behaviors of an ultracapacitor can serve a valuable role when optimizing the design of future cells [18].

Many models are available for modeling the complex behavior of an ultracapacitor and the most widely used ones are based on porous electrode theory [18]. Models based on porous electrode theory accurately predict the ultracapacitor performance by solving a series of governing equations. There also exist other equivalent circuit models such as classical equivalent circuit which is composed of a capacitor, an equivalent parallel resistance, and an equivalent series resistance to model the electrical behavior of the ultracapacitor. This model can also be used to accurately predict the ultracapacitor's dependence on frequency by employing multiple time constants [18]. In slow discharge applications on the order of a few seconds, the classical equivalent circuit for an ultracapacitor can adequately describe capacitor performance. The time constants in an electrical circuit can be generated by adding a resistor-capacitor branch and the

values of which need to be determined from electrochemical impedance spectroscopy measurements.

The proposed electrical model consists of three resistor-capacitor (RC) branches to achieve a better fit to the collected data on the electrical behavior of an ultracapacitor than the classical equivalent circuit. The capacitance in each pore of porous electrodes can be modeled as an RC transmission line [18].

In this chapter, modeling and simulation of electrical behavior of graphene-based ultracapacitors are discussed. The proposed electric model for ultracapacitor modeling is also presented. A three-branch RC circuit model is employed to calculate the electrical behavior of the ultracapacitor. Also the mathematical model used in the simulation process has been presented followed by the simulation as well as the discussion of the simulated results. The validation of the modeling approach is provided through the comparison of the modeling results with the experimental measurements.

## **4.2 Proposed Electric Model for Ultracapacitors**

An overview of this work combined with an analysis of the experimental data shows that the ultracapacitor electric model has to take into account many phenomena which are as follows:

- the ultracapacitor behavior depends on many physical parameters; however, we consider the parameters to be basically voltage and temperature;
- an equivalent *RC* transmission line behavior that characterizes the ultracapacitors dynamic response especially in the [0.1 Hz; 10 Hz] frequency range. This behavior is induced by the porous nature of the capacitive interface;

- a resonance frequency ( $<200$  Hz) that corresponds to a transition between capacitive and inductive nature of the impedance and measured at the minimum of the real part of the impedance;
- a charge redistribution phenomenon that occurs at low frequencies or for charge and discharge higher than 1 min. It is modeled by two  $RC$  branches that are characterized by long time constants compared with the time constant of the  $RC$  transmission line;
- a self-discharge which can be modeled by a high parallel resistor called leakage resistor.

Therefore, a general electrical model is proposed in Figure 4.1. But, according to the goal of this research, some phenomena can be neglected in order to use the most suitable and the least complicated electric model.

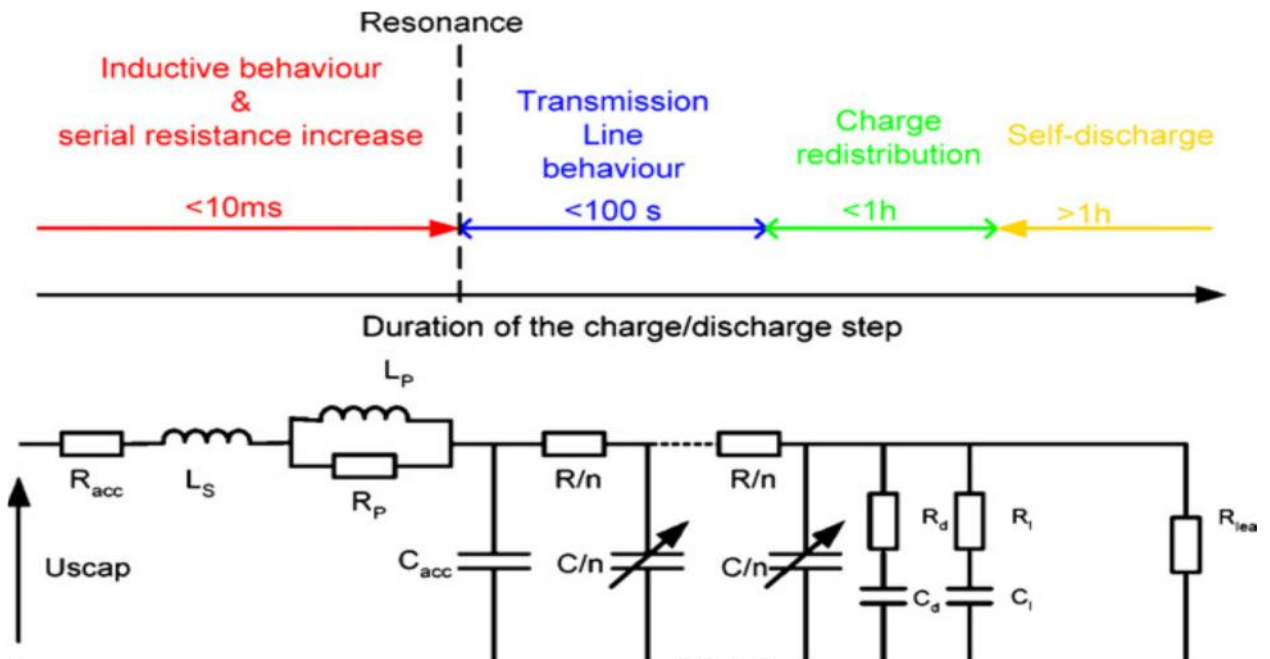


**Figure 4.1** General electric model of ultracapacitor (Ladder Network).  
Source:[18].

The aim is to provide a window of time-observation of the current and voltage that is needed for the simulation. Therefore, the charge redistribution and the self-discharge phenomena will be neglected. Also, the high frequency behavior will not be modeled. So, the proposed RC parallel branch electric model in this work will simulate the electrical behavior of graphene-based ultracapacitor cell as shown in Figure 4.2.

In order to ensure the simplicity and accuracy of the model, three RC branch models were chosen, although a large number of RC branches may be favorable to capture the nonlinear electrical behaviors of ultracapacitors. Each of the three branches has a distinct time constant differing from the others. The immediate branch with the elements  $R_1$  and  $C_1$  dominates the immediate behavior in order of a few seconds. The delayed branch with the elements  $R_2$  and  $C_2$  dominates the immediate behavior in the range of minutes. The long-term branch with the elements  $R_3$  and  $C_3$  dominates the behavior for times longer than ten minutes. To set up a practical engineering model in the present work, the nonlinear capacitance effect is included only in one RC element. Instead of adding an additional voltage-dependent capacitor branch in parallel with immediate branch capacitor as in [8, 18],  $R_1$  and  $C_1$  were made current-dependent.

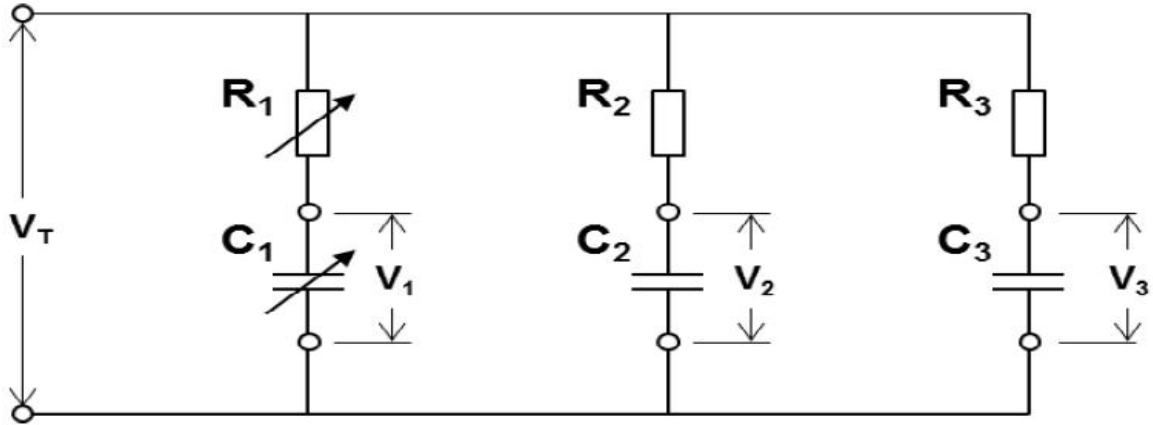


**Figure 4.2** Three resistor-capacitor (RC) parallel branch model  
Source: [8].

### 4.3 Simulation Environment

The system scale simulation of the electrical behavior of the ultracapacitor cell was developed in Matlab/Simulink environment. Simscape is a Matlab based tool that enables the users to model Electrical and Mechanical systems as physical networks. Simscape technology automatically constructs equations that characterize the behavior of the system.

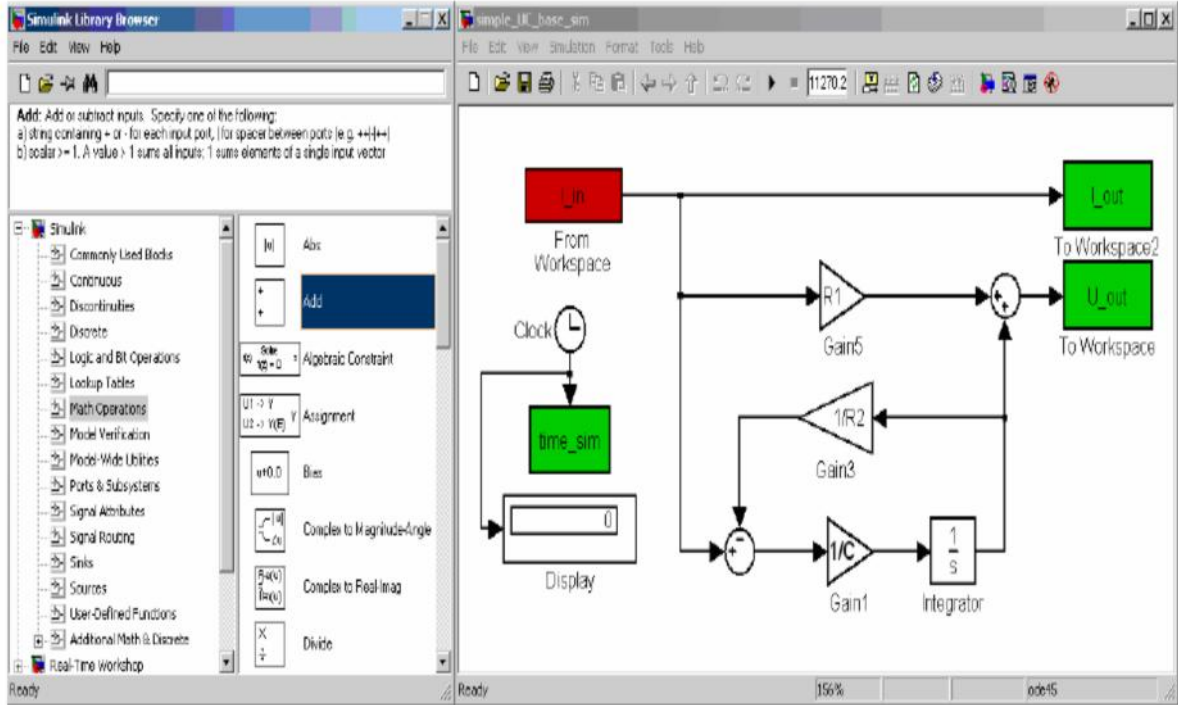


**Figure 4.3** User interface for Simulink  
Source: Matlab/simulink version (2014 a).

#### 4.4 Mathematical Model

Since the voltage across each branch is equal to the terminal voltage of the ultracapacitor shown in Figure 4.2, the following equation can be written for each branch:

$$V_T = i_1 R_1 + V_1 = i_2 R_2 + V_2 = i_3 R_3 + V_3 \quad (4.1)$$

where  $V_T$  is the terminal voltage (V) of the ultracapacitor cell;  $i_1$ ,  $i_2$ ,  $i_3$  are the currents (A) flowing through the first, second, and third branches of Figure 4.2, respectively;  $R_1$ ,  $R_2$ ,  $R_3$  are the resistances ( $\Omega$ ) of the first, second, and third branches of Figure 4.2, respectively; and  $V_1$ ,  $V_2$ ,  $V_3$  are the capacitor voltages (V) of the first, second, and third branches of Figure 4.2, respectively. The currents flowing through first, second, and third

branches of Figure 4.2 are given as the multiplication of the branch capacitance and the time derivative of branch capacitor voltage as follows:

$$i_1 = C_1 \frac{dV_1}{dt} \quad (4.2)$$

$$i_2 = C_2 \frac{dV_2}{dt} \quad (4.3)$$

$$i_3 = C_3 \frac{dV_3}{dt} \quad (4.4)$$

where,  $C_1$ ,  $C_2$ ,  $C_3$  are the capacitances (F) of the first, second, and third branches of Figure 4.2, respectively; and  $t$  is the time (s). Alternatively, these currents can be obtained from Equation (4.1) as follows:

$$i_1 = \frac{V_T - V_1}{R_1} \quad (4.5)$$

$$i_2 = \frac{V_T - V_2}{R_2} \quad (4.6)$$

$$i_3 = \frac{V_T - V_3}{R_3} \quad (4.7)$$

Because the terminal current of the ultracapacitor is equal to the summation of the three branch currents, the following equation for the terminal current can be written as:

$$I = i_1 + i_2 + i_3 \quad (4.8)$$

where,  $I$  is the terminal current (A) of the ultracapacitor. By substituting Equations (4.2)–(4.4) and Equations (4.5)–(4.7) into Equation (4.8), the following equations for the branch capacitor and terminal voltages can be derived as follows:

$$\frac{dV_1}{dt} = \frac{V_1(R_T - R_1)}{R_1^2 C_1} + \frac{V_2 R_T}{R_1 R_2 C_1} + \frac{V_3 R_T}{R_1 R_3 C_1} + \frac{I R_T}{R_1 C_1} \quad (4.9)$$

$$\frac{dV_2}{dt} = \frac{V_1 R_T}{R_1 R_2 C_2} + \frac{V_2 (R_T - R_2)}{R_2^2 C_2} + \frac{V_3 R_T}{R_2 R_3 C_2} + \frac{I R_T}{R_2 C_2} \quad (4.10)$$

$$\frac{dV_3}{dt} = \frac{V_1 R_T}{R_1 R_3 C_3} + \frac{V_2 R_T}{R_2 R_3 C_3} + \frac{V_3 (R_T - R_3)}{R_3^2 C_3} + \frac{I R_T}{R_3 C_3} \quad (4.11)$$

$$V_T = \frac{V_1 R_T}{R_1} + \frac{V_2 R_T}{R_2} + \frac{V_3 R_T}{R_3} + I R_T \quad (4.12)$$

$$\frac{1}{R_T} = \frac{1}{R_1} + \frac{1}{R_2} + \frac{1}{R_3} \quad (4.13)$$

where,  $R_T$  is the equivalent resistance ( $\Omega$ ) of three parallel branches. The parameters used to calculate the electrical behavior of the ultracapacitor are given in Table 4.1. As mentioned previously,  $C_1$  and  $R_1$  are dependent on the terminal current,  $I$ , while  $C_2$ ,  $C_3$ ,  $R_2$ , and  $R_3$  are made constant. The parameter values are chosen to provide the best fit of the modeling results to the experimental data [8].

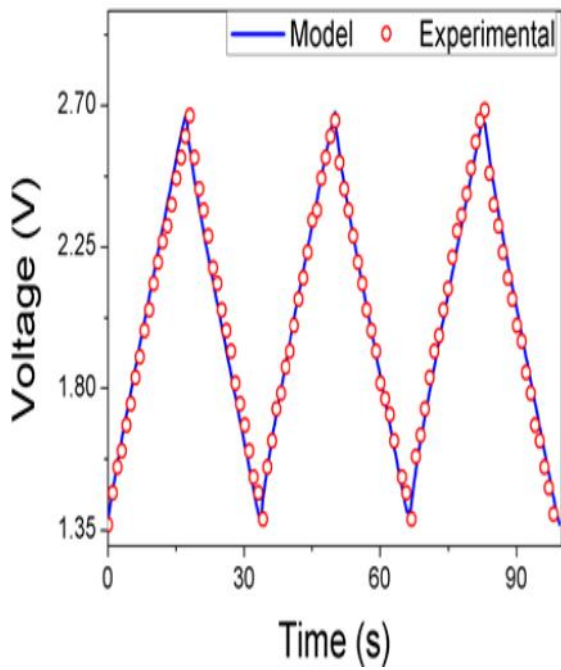
**Table 4.1** Parameters used to calculate the electrical behavior of the Ultracapacitor

Parameter ( unit)	50 A Cycling	100 A Cycling	150 A Cycling	200 A Cycling
$C_1$ ( F )	$4.22 \times 10^2$	$3.80 \times 10^2$	$3.70 \times 10^2$	$3.30 \times 10^2$
$C_2$ ( F )	$2.07 \times 10^2$	$2.07 \times 10^2$	$2.07 \times 10^2$	$2.07 \times 10^2$
$C_3$ ( F )	$1.40 \times 10^1$	$1.40 \times 10^1$	$1.40 \times 10^1$	$1.40 \times 10^1$
$R_1$ ( $\Omega$ )	$6.49 \times 10^{-4}$	$4.00 \times 10^{-4}$	$3.60 \times 10^{-4}$	$2.80 \times 10^{-4}$
$R_2$ ( $\Omega$ )	$1.00 \times 10^{-2}$	$1.00 \times 10^{-2}$	$1.00 \times 10^{-2}$	$1.00 \times 10^{-2}$
$R_3$ ( $\Omega$ )	$2.31 \times 10^{-2}$	$2.31 \times 10^{-2}$	$2.31 \times 10^{-2}$	$2.31 \times 10^{-2}$

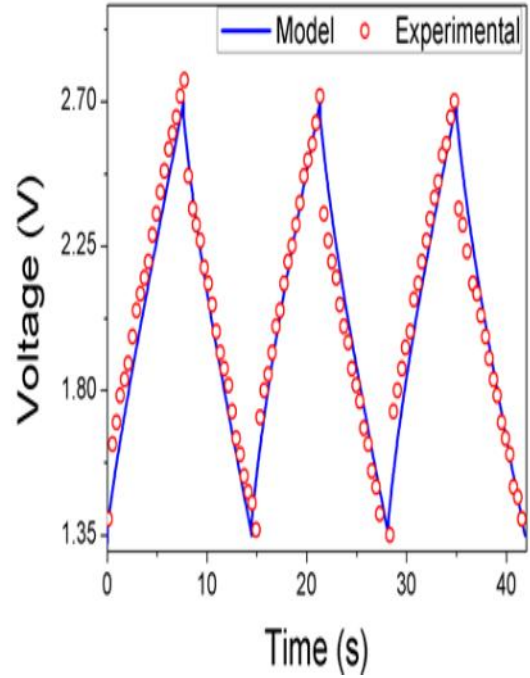
## 4.5 Results and Discussion

In order to validate the quantitative modeling approach adopted in this work with high current rate, the performance characteristics of the ultracapacitor cell was simulated during cycling and compared with the voltage response of the model to the experimental response obtained from a 2.7 V/650 F ultracapacitor cell. The specific current and voltage profile of up to 200A and 18V, respectively, were obtained during charge and discharge times. By modifying the duration of the charge and discharge times, one can estimate the precision of the model for different voltage variations. This result shows that, after 1000 s, there is no global divergence between measured and calculated points. Also, a good matching at the time scale of few seconds was observed.

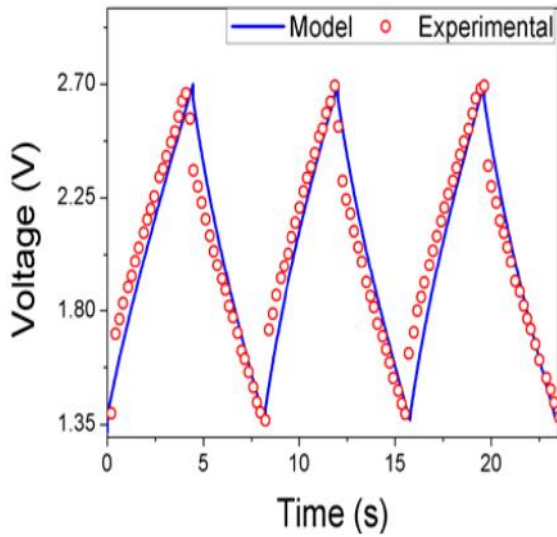
The ultracapacitor was subject to the constant-current charge and discharge current cycles between the half-rated voltage (1.35 V) and the rated voltage (2.7 V). The charge/discharge current values examined were 50, 100, 150, and 200 A. The solutions to Equations (4.1)–(4.4) were obtained by using “ode45” solver of MATLAB. The modeling results for the variations of the ultracapacitor cell voltages, as a function of time, for different charge/discharge currents are compared with the experimental data in Figure 4.4. The modeling results shown in Figure 4.4 are in good agreement with the experimental measurements.



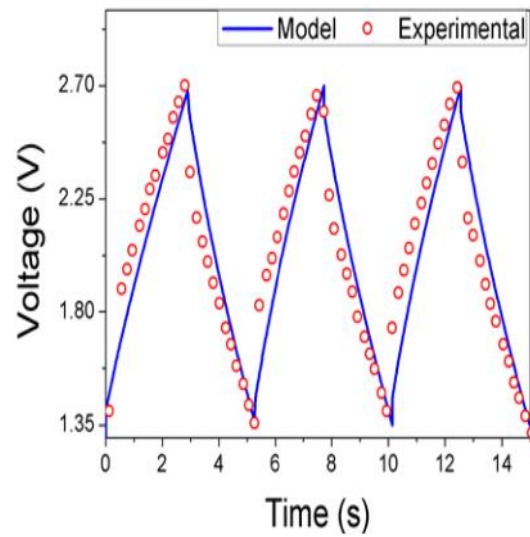
( a )



( b )



( c )



( d )

**Figure 4.4** Comparison between the modeling results and experimental data for the variations of the ultracapacitor cell voltages as a function of time at various charge/discharge currents of: (a) 50; (b) 100; (c) 150; and (d) 200 A.

Simulation results for Voltage-Time and Voltage-Current at various current densities were also obtained and plotted for graphene-based ultracapacitors and the results are shown in Figure 4.5 and 4.6 below.

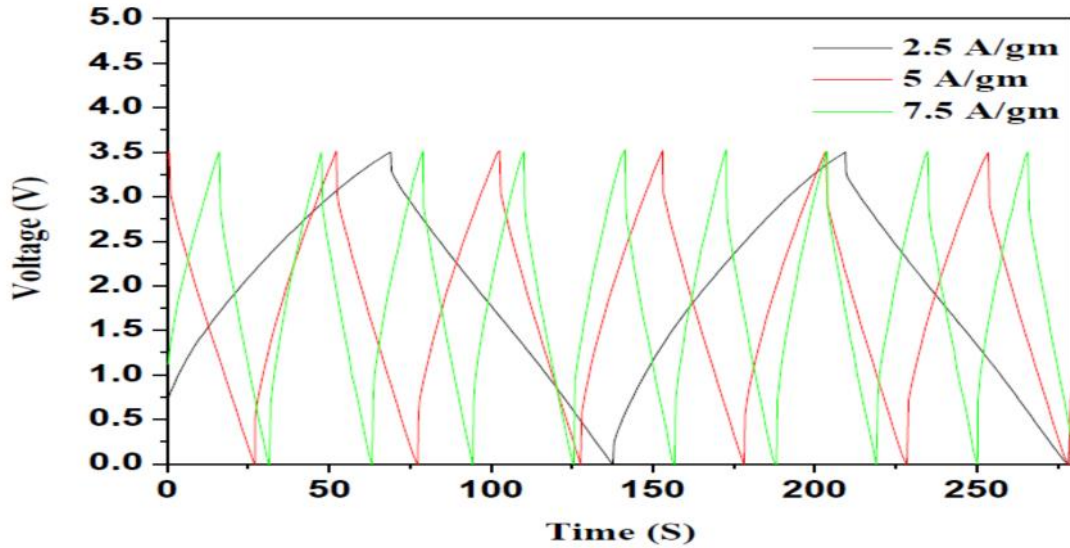


**Figure 4.5** Charge/discharge curve for graphene ultracapacitor at various current densities  $2.5 \text{ Ag}^{-1}$ ,  $5 \text{ Ag}^{-1}$ ,  $7.5 \text{ Ag}^{-1}$ .

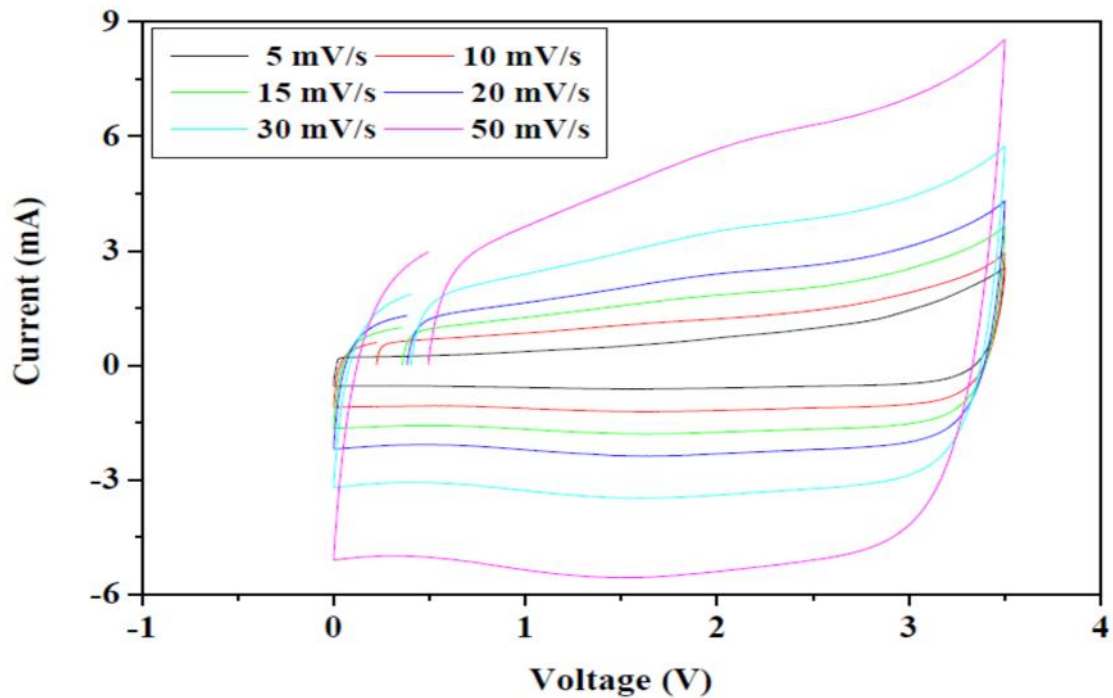


**Figure 4.6** Current –Voltage curves of graphene-based ultracapacitor.

### 4.5.1 Varying Voltage Test

To better analyze the electrical behavior of graphene-based ultracapacitors, a new test is designed based on the procedure used in screening test. Instead of always charging to the rated voltage, this test uses charges that reach different voltage levels. During the cycle, the ultracapacitor is charged to different increasing voltage levels. The reason for charging to different voltages is to be able to see how the ultracapacitor behavior is affected by varying the voltage levels. Between each charge, a discharge is done so that charging always starts from the same level. This charging cycle is then repeated using different current levels. During the first cycle, the ultracapacitor is charged to three different voltage levels but when the current increases, the lowest voltage level only consists of losses in the series resistance. Because of this, the low voltage level is excluded from the high current test. The resulting voltage curve is shown in Figure 4.7.

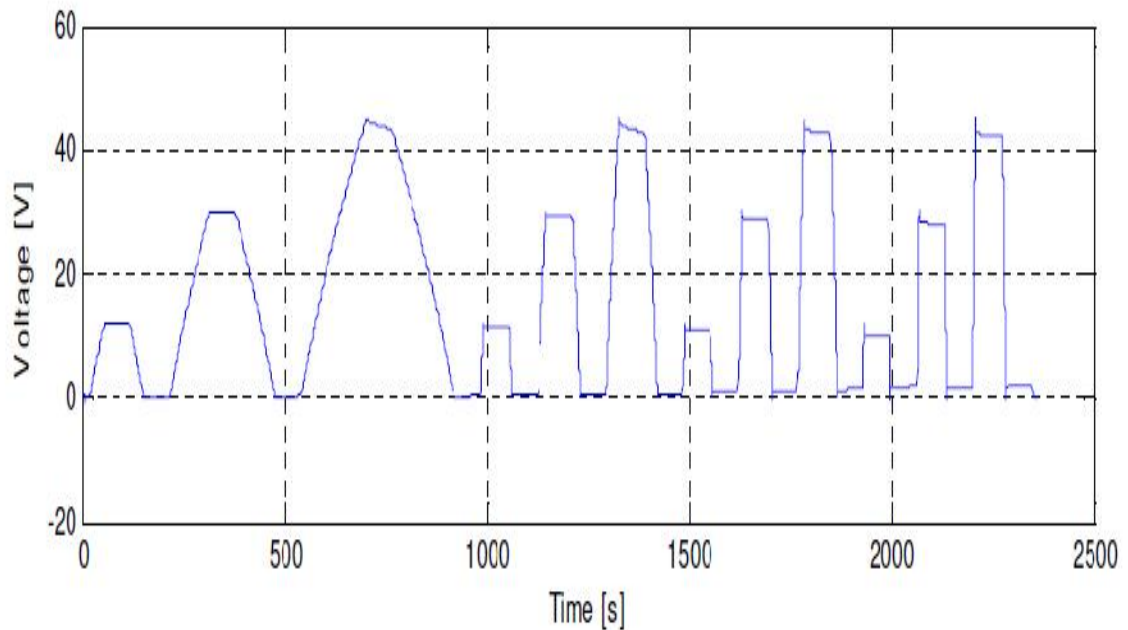


**Figure 4.7** Voltage curve for multiple voltages and currents simulations

## CHAPTER 5

### CONCLUSIONS AND FUTURE WORK

#### 5.1 Summary

The design and simulation of electrical behavior of graphene-based ultracapacitor was discussed. A mathematical procedure was developed to study the electrical behavior of a 2.7 V/650 F ultracapacitor cell during constant-current charge/discharge cycling between the half-rated voltage and the rated voltage. A three RC parallel branch model is employed to calculate the electrical behavior of the ultracapacitor. The modeling results for the variations of the ultracapacitor cell voltage, as a function of time, for different charge/discharge currents of 50, 100, 150, and 200A are in good agreement with the experimental measurements.

The investigation of the electrical behavior of the ultracapacitors is a preliminary step before their integration in real applications. The model has to be completed with temperature dependent parameters. This study has to be completed with thermal and reliability studies as high current rates lead to self-heating and ageing.

A particular emphasis was placed here on the latest developments of carbon-based materials that are used to fabricate solid-state (both flexible and rigid) ultracapacitors. A major challenge remains to increase the thickness of the active materials (i.e., 3D structures) in order to increase the specific capacitance and energy density of a ultracapacitor, without sacrificing the cyclic stability and power densities in a given footprint for future ultracapacitor design. Material constraints are required because the

long-term goal is to produce on-chip devices. A number of directions such as electrode materials were identified and it required further improvements.

Integrating new carbon nanomaterials such as CNTs and graphene into ultracapacitors would be a good choice to improve specific surface area, capacitance and energy storage. These nanomaterials not only can be directly used as electrodes but also could be used as nanotemplates for pseudocapacitive materials to further increase their utilization efficiency and more importantly to solve the long-term cyclic problem associated with volume change and swelling during the ion doping/undoping process.

## REFERENCES

1. Alcicek, G., et al. (2007). Experimental study of temperature effect on ultracapacitor ageing. Power Electronics and Applications, 2007 European Conference on, IEEE.
2. Bunch, J. S. (2008). Mechanical and electrical properties of graphene sheets, Cornell University.
3. Chen, J., et al. (2002). "Electrochemical characterization of carbon nanotubes as electrode in electrochemical double-layer capacitors." Carbon **40**(8): 1193-1197.
4. Conway, B. E. (1991). "Transition from "supercapacitor" to "battery" behavior in electrochemical energy storage." Journal of the Electrochemical Society **138**(6): 1539-1548.
5. Costescu, R. M., et al. (2003). "Thermal conductance of epitaxial interfaces." Physical Review B **67**(5): 054302.
6. Halper, M. S. and J. C. Ellenbogen (2006). "Supercapacitors: A brief overview." The MITRE Corporation, McLean, Virginia, USA: 1-34.
7. Johansson, P. and B. Andersson (2008). "Comparison of simulation programs for supercapacitor modelling." Master of Science Thesis. Chalmers University of Technology, Sweden.
8. Lee, J., et al. (2014). "Modeling of the Electrical and Thermal Behaviors of an Ultracapacitor." Energies **7**(12): 8264-8278.
9. Miller, J. R. and P. Simon (2008). "Fundamentals of electrochemical capacitor design and operation." Electrochemical Society Interface **17**(1): 31-32.
10. Min, K. and N. Aluru (2011). "Mechanical properties of graphene under shear deformation." Applied Physics Letters **98**(1): 013113.
11. Oakes, L., et al. (2013). "Surface engineered porous silicon for stable, high performance electrochemical supercapacitors." Scientific reports **3**.
12. Park, S., et al. (2008). "Graphene oxide papers modified by divalent ions—enhancing mechanical properties via chemical cross-linking." Acs Nano **2**(3): 572-578.
13. Pop, E., et al. (2012). "Thermal properties of graphene: Fundamentals and applications." MRS bulletin **37**(12): 1273-1281.

14. Schiffer, J., et al. (2006). "Heat generation in double layer capacitors." Journal of Power Sources **160**(1): 765-772.
15. Sharma, P. and T. Bhatti (2010). "A review on electrochemical double-layer capacitors." Energy Conversion and Management **51**(12): 2901-2912.
16. Simon, P. and Y. Gogotsi (2008). "Materials for electrochemical capacitors." Nature materials **7**(11): 845-854.
17. Stoller, M. D., et al. (2008). "Graphene-based ultracapacitors." Nano letters **8**(10): 3498-3502.
18. Tammineedi, C. (2011). MODELING BATTERY-ULTRACAPACITOR HYBRID SYSTEMS FOR SOLAR, The Pennsylvania State University.
19. Tecate Group (May 1,2015). "What is an Ultracapacitor", [www.tecategroup.com](http://www.tecategroup.com).
20. Wang, G., et al. (2012). "A review of electrode materials for electrochemical supercapacitors." Chemical Society Reviews **41**(2): 797-828.
21. Xiong, G., et al. (2014). "A Review of Graphene-Based Electrochemical Microsupercapacitors." Electroanalysis **26**(1): 30-51.

Johansson, P. and B. Andersson (2008). "Comparison of simulation programs for supercapacitor modelling." Master of Science Thesis. Chalmers University of Technology, Sweden.